UNIVERSITY OF SOUTHAMPTON

Aerodynamics and Aeroacoustics of Slat Tracks

by

Bidur Khanal

Submitted for MPhil

School of Engineering Sciences

Aerodynamics and Flight Mechanics Group

April 2009

UNIVERSITY OF SOUTHAMPTON

<u>ABSTRACT</u>

SCHOOL OF ENGINEERING SCIENCES
AERODYNAMICS AND FLIGHT MECHANICS GROUP

Aerodynamics and Aeroacoustics of Slat Tracks

by Bidur Khanal

An overview on the progress of the research work on the aerodyamics and aeroa-coustics of a three-dimensional multi-element wing with slat track is presented. A two step computational procedure which involves the solution of Navier-Stokes equations in the first step and an integral surface solution of the Ffowcs-Williams and Hawkings equation in the subsequent step, is used to predict the far-field noise. Two main approaches are used for the computational work in this project. Firstly, the simulations based on the Linearized Euler Equations and the Acoustic Perturbation Equations are used in two- and three-dimensions to understand the effect of the slat track on the acoustic wave propagation. Dipoles and quadrupole are used as the simulated acoustic source. Also the effect of the mean flow in the wave propagation is studied by including a background mean flow in the APE sim-ulations. An integral solution of FW-H equation is used for the far-field acoustic prediction after the source computation. The results are analysed and the future work is proposed.

Acknowledgements

I would like to thank Professor Xin Zhang for his continuous guidance and support, without him I would not have been able to complete this research study. I would also like to thank Zhaokai Ma for all his helps and supports. Thanks to Professor GM Lilley for his continuous encouragement to complete this thesis and Dr Sammie Chan for his continuous helps and company. Thanks must also go to Dr Jae Wook Kim for his ever-open door and helpful advices and; all my colleagues in Southampton office Tizzard/Room 5073.

Finally, I am thankful to my wife Rita for her continuous support and understanding during this thesis writing-up period.

Authors declaration

I, Bidur Khanal declare that this MPhil thesis on *Aerodynamics and Aeroacoustics of Slat Tracks* and the work presented in it, are my own. I, here by, confirm that:

- This work was done during my candidature as a research student at this University.

- Where I have quoted from the work of others, the source is clearly given. With the exception of such quotations, this work is entirely my own.

- I have always clearly stated all published and unpublished works of others wherever I consulted them.

- I have acknowledged all the main sources of help.

- For the works I did jointly with others, I have made clear about the contributions of others and mine.

Contents

List of Figures

List of Tables

Nomenclature

All units are in SI

Alphanumeric

a_0 Speed of sound in ambient air

c Fully retracted wing chord

C_p Pressure coefficient; $(p - p_\infty)/\frac{1}{2}\rho_\infty U_\infty^2$

f Frequency

g_s Slat gap

H Heavy-side function

L_i Aeroacoustic loading term

M Mach number

o_s Slat overlapp

p Static pressure

p_{gauge} Gauge pressure

p_{ij} Compressive stress tensor

r Radial distance from an acoustic source

St Strouhal number

T Static temperature

t Time

T_{ij} Lighthill's stress tensor

U Velocity in x-direction

u, v, w Velocity components in Cartesian coordinates

U_n Aeroacoustic thickness term

x, y, z Cartesian coordinate system

$\mathbf{s}$ Displacement vector

$\mathbf{v}$ Velocity vector

Re   Reynolds number

Greek Symbols

δ_{ij} Dirac delta function

δ_s Slat deflection angle

$\frac{\nu_t}{\nu}$ Freestream turbulence viscosity ratio

γ Ratio of specific heats, 1.4

μ Coefficient of viscosity

ν Kinematic viscosity

Ω Vorticity

ρ Fluid density

Symbols

$\langle \rangle$ Time averaged quantity

Subscripts

$()'$ Perturbation value

$()_\infty$ Freestream value

$()_{rms}$ Root mean square value

Abbreviations

2D   Two-dimensional

3D   Three-dimensional

AIAA	American Institute of Aeronautics and Astronautics
APE	Acoustic Perturbation Equations
CAA	Computational Aeroacoustics
CFD	Computational Fluid Dynamics
DES	Detached Eddy Simulation
DRP	Dispersion Relation Preserving
FFT	Fast Fourier Transform
FWH	Ffowcs Williams-Hawkings
LEE	Linearised Euler Equations
NASA	National Aeronautics and Space Administration
PIV	Particle Imaging Velocimetry
PPW	Points per Wavelength
RANS	Reynolds-Averaged Navier-Stokes
SA	Spalart-Allmaras
SPL	Sound Pressure Level
URANS	Unsteady Reynolds-Averaged Navier-Stokes

Chapter 1

Introduction

The importance of reducing airframe noise during approach has now become apparent to the international research community. Civil air traffic continues to increase as does pressure from the public to control the resulting increase in the noise by aircraft. Aircraft noise is particularly annoying to those living in close proximity to airports. It is clear that noise reduction technology is critical to the future development and operation of the world air transportation system. It is anticipated that with the projected increase in air travel aeroacoustics research will be more critical for the certification of future aircraft. Many organizations in governments and industries all over the world have taken major strides in preparing plans for reducing aircraft noise. This includes noise emanating from the airframe components such as leading edge slat, slat tracks, flaps etc; and engine components such as the fan, compressor, combustor, turbine and last but not least, jet exhaust noise (both subsonic and supersonic). In addition, noise issues are increasingly important on account of both environmental and structural concerns. The latter concern cannot be ignored for the worlds aging aircraft fleet. Higher acoustic loads on aircraft translates to more expense and more weight for reinforced aircraft structures [1]. Therefore airframe noise has become an important consideration from civil certification, environmental as well as structural view point.

The aim of this research project is to study the noise generated by slat tracks. The project will focus mainly on computational simulation. A two step procedure is used to simulate the flow field and understand noise generation and propagation phenomena. Firstly nearfield simulations using linearised equations with source modelling are performed in both 2D and 3D configurations to study the effect of slat tracks on sound wave propagation. The farfield acoustic solution is then extracted using an integral solution of the Ffowcs-Williams and Hawkings equation

[2]. The linearized simulations are performed using a high order computational aeroacoustic (CAA) solver. Full Navier-Stokes simulations were also performed to extract the mean flowfields. The extracted mean flow was then input to the linearized solver to study the effects of background mean flow on wave propagation.

1.1 Geometry

This project is concerned with the study of noise generated by slat tracks. Slat tracks are support rails which support structurally and allow the deployment and retraction of leading edge slat on a multi-element aircraft wing. A typical multi-element wing consists of a leading edge slat, a main wing and a trailing edge flap. A generic multi-element wing without slat track is shown in Figure 1.1. Figure 1.1 shows a multi-element wing with a slat track.
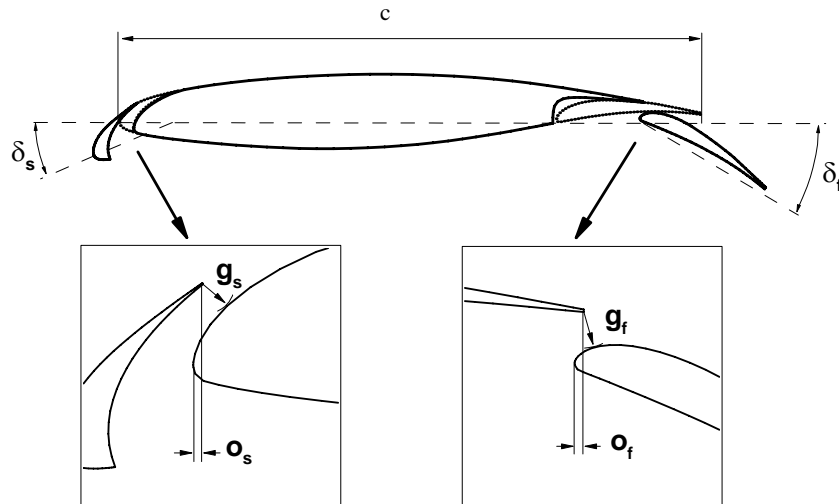
FIGURE 1.1: A generic wing profile with nomenclature. (Courtsey of Zhaokai Ma)

1.2 Aims

The aim of this research project is to identify the contribution of the noise from slat tracks on the noise generated by the slat and to develop a suitable noise reduction treatment. Computational methods will be used as the main tool in this research. Several activities set out to achieve the aims are summarised below:
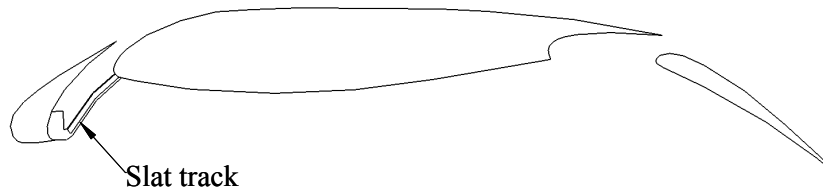
FIGURE 1.2: Slat track in a multi-element wing. (Courtsey of Airbus UK)

- The presence of the slat track causes the noise from other sources (e.g. slat trailing edge noise, broadband noise due to shear layer fluctuation at the slat cusp etc) to reflect and diffract. Hence, the main aim of this research project is to study these effects of the slat track.

Chapter 2

Review of Past Research

This chapter gives a literature review relavant to the current research. This includes computational methodologies, computational solvers and the advances in the leading edge slat noise research.

2.1 Introduction

The study of aeroacoustics is mainly concerned with noise produced by aerodynamic sources including turbulence and moving aerodynamic surfaces. An integral component of the acoustic analysis of these sources is the aerodynamic field generated by them, which in essence, acts as the source of noise. Also aeroacoustics is concerned essentially with a small by-product of fluid flows whose internal dynamics can generally be assumed to be negligibly small. This initially gives rise to the hope that the flow dynamics will be more or less decoupled from the wave motion and hence an assumed knowledge of the flow can be used to predict the wave motion. However, flow variables defining a turbulent flow can not be defined with any degree of confidence which then suggests that the aeroacoustic theory should be formulated in such a way that it demands the minimum information from the flow. Hence great care is needed while approximating the aerodynamically generated noise. Firstly it is a small by-product of the aerodynamic flow field. Secondly even though the approximations regarding the aerodynamic field may be safe enough, they can be fatal for the by-product. Large errors are, hence, likely even with reasonable approximations. This is one of the reasons why the field of aeroacoustics is one of the most challenging areas in engineering research.

With significant quietening of modern, high by-pass-ratio turbofan engines, airframe noise competes with engine noise. During final approach, engine noise and airframe noise are comparable in level [3, 4, 5]. Recent work of Lilley [6] stated that the noise from the airframe, is prominent during approach, due entirely to successes in reducing engine noise. This also means that further reduction in noise can only be achieved if both engine and airframe noise are reduced. A noise reduction of 10dB seems a small reduction, represents a reduction in the measured acoustic power by 90 percent. Yet because of the logarithmic response of human ear, 10dB represents only a modest reduction. Airframe noise is most pronounced during aircraft approach because engines are operating at reduced thrust and high lift devices and landing gears are deployed at the same time. A study by Davy *et al.* [7] on a small scale model airbus aircraft model indicated that high lift devices and landing gear are the main sources of airframe noise when the aircraft is configured for approach. During approach, aircraft travel through shallow glide angles, hence flying at low elevation for a considerable distance near to airports. This exposes ground communities to extended durations of higher noise. It is, therefore, important to control the noise generated by these deployed devices in order to reduce the aircraft noise signature to the local urban area. The negative effects of aircraft noise on urban areas and communities near to the airport can severely affect the future growth in civil air travel. Hence aerodynamically generated noise control has emerged to be a challenging task for aeronautical engineers.

This project is, hence, an effort to contribute towards the on-going aeroacoustic research in high lift devices. Specifically, it is concerned with the investigation of noise generated by slat tracks in a fully deployed condition (see Figure 2.1). Although there has been a significant amount of work in the sound generated by slats in both two- and three-dimensional configurations, little has been done in the case of noise from slat tracks. This chapter gives a summary of the literature. Only very few past works explicit to slat track aeroacoustics are found. Nonetheless a number of publications in slat aeroacoustics has been cited which is close enough to establish a background for the advancement of the slat track aeroacoustic project.

Aerodynamic noise research is an evolving subject. It has a history of about 50 years as a challenging problem of technology and a reputed subject for study. It was Lighthill's paper in early 1950s which for the first time demonstrated how a subject could progress when the physical problems associated with it were properly modelled and analysed. This was a leap for development of modern aeroacoustic approach, in which theory and experiment are two inseparable parts of aeroacoustic research. Lighthill [8] established the theory of aerodynamic noise,

which was based on exact Navier-Stokes equations. However, the answer obtained from Lighthill's theory is only as accurate as the equivalent acoustic source terms, which must be calculated or measured for the given unsteady or turbulent flow. In Lighthill's equation the acoustic sources are treated as a distribution of equivalent point sources, whose strengths are obtained from Lighthill's stress tensor T_{ij}, where T_{ij} is derived from the properties of the unsteady or turbulent flowfield. The theory assumes the absence of solid boundary and hence insignificant back reaction of the sound produced on the flowfield itself (i.e. the sound produced is so weak relative to the motions producing it that no significant flow-acoustic interaction can be expected). Lighthill's mathematical formulation to model the acoustic propagation can be represented by the following non-homogeneous equation:

$$\frac{\partial^2 \rho}{\partial t^2} - a_0^2 \nabla^2 \rho = \frac{\partial^2 T_{ij}}{\partial x_i \partial x_j}. \tag{2.1}$$

Where, $T_{ij} = (\rho v_i v_j + p_{ij} - a_0^2 \rho \delta_{ij})$. and a_0 is the speed of sound in ambient air. Lighthill solved above wave equation using properties of generalised functions [9], the final solution is presented below:

$$\rho - \rho_0 = \frac{1}{4\pi a_0^2} \frac{\partial^2}{\partial x_i \partial x_j} \int_V \frac{T_{ij}(y, t - \frac{r}{a_0})}{r} dy. \tag{2.2}$$

Also this theory assumes that sound is radiated into free space. However, when the source mean flow is non-uniform the propagation of sound waves through it involves flow-acoustic interaction [10]. Hence this theory is most applicable to the analysis of energy emitted from subsonic flows as sound, and not to the study of the change in character of generated sound which is often observed in transitions to supersonic flow due to high frequency emission associated with shock waves.

Curle [11] extended the Lighthill's theory to account for the effect of solid boundaries. Curle pointed out that the presence of solid boundaries can affect the acoustic propagation in two ways:

Firstly, the sound produced by quadrupole sources in Lighthill's theory will be reflected and diffracted by the solid boundary. Secondly and most importantly the quadrupoles will no longer be distributed over the whole of the space but only the region external to the solid boundary. It is therefore possible to have a resultant distribution of dipoles (or monopole sources) at the boundaries. Dipoles are especially likely since in acoustics they correspond to the externally applied forces and such forces are present between the fluid and the solid boundary. The modified version of the Lighthill's solution proposed by Curle which now consists

of volume as well as surface integral is,

$$\rho - \rho_0 = \frac{1}{4\pi a_0^2} \frac{\partial^2}{\partial x_i \partial x_j} \int_V \frac{T_{ij}(y, t - \frac{r}{a_0})}{r} dy - \frac{1}{4\pi a_0^2} \frac{\partial}{\partial x_i} \int_S \frac{P_i(y, t - \frac{r}{a_0})}{r} dS(y). \quad (2.3)$$

Where,

$$P_i = -\ell_j P_{ij}.$$

ℓ_j is the direction cosine of the outward normal to the fluid. In Curle's solution an extra surface integral is included which is equivalent to the sound generated by a distribution of dipoles of strength P_i per unit area in a medium at rest(P_i is exactly the force per unit area exerted on the fluid by the solid boundaries in the x_i direction). Also the volume integral in Curle's equation is different from the Lighthill's equation. The difference represents the effect of the impact (on solid boundary) of sound waves from the quadrupoles. Curle, hence, proposed the sound field as the sum of that generated by a volume distribution of quadrupoles and by the source distribution of dipoles.

Curle's formulation was not still suitable for the aerodynamic noise problems which consisted moving surfaces and hence Ffowcs-Williams and Hawkings [2] extended the Lighthill-Curle theory to evaluate the density field radiated by turbulence in the presence of arbitrarily moving surfaces which when expressed in terms of generalised functions [9] is:

$$\left(\frac{\partial^2}{\partial t^2} - a_0^2 \nabla^2 \right) (\rho H(f)) = \frac{\partial^2}{\partial x_i \partial x_j} (T_{ij} H(f)) - \frac{\partial}{\partial x_i} (L_i \delta(f)) + \frac{\partial}{\partial t} (U_n \delta(f)). \quad (2.4)$$

Where,

$$T_{ij} = \rho u_i u_j - \tau_{ij} + [(p - p_0) - c_0^2(\rho - \rho_0)] \delta_{ij}.$$

$$L_i = L_{ij} \hat{n}_j = \left[\rho u_i(u_j - v_j) + p'_{ij} \right] \hat{n}_j.$$

$$U_n = U_i \hat{n}_i = \left[\rho(u_i - v_i) + \rho_0 v_i \right] \hat{n}_i.$$

$$p'_{ij} = (p - p_0)\delta_{ij} - \tau_{ij}.$$

In aeroacoustic literature, the three terms on the right hand side of above equation are known as quadrupole, loading and thickness source terms respectively. The thickness and loading source terms are surface distribution of sources as indicated by $\delta(f)$. When the control surface encloses a physical surface, the thickness source accounts for the displacement of fluid produced by the body and the loading source accounts for the unsteady loading exerted by the body on the fluid. The quadrupole source, a volume source distribution as indicated by $H(f)$, accounts

for all the non-linearity in the region external to the control surface. Solutions to the above equation can be presented in various forms. Below is one of the frequently used forms (a detailed derivation is given in [12]).

$$
\begin{aligned}
c_0^2 \left(\rho - \rho_0\right) H(f) \;=\; & \frac{\partial^2}{\partial x_i \partial x_j} \int_V \left[\frac{T_{ij}}{r \left|1 - M_r\right|}\right]_{\tau^*} \mathrm{d}V \;+\; \int_S \left[\frac{Q_r \dot{+} Q_r}{r \left(1 - M_r\right)^2}\right]_{\tau^*} \mathrm{d}S \\
& +\; \frac{1}{c_0} \int_S \left[\frac{F_r}{r \left(1 - M_r\right)^2}\right]_{\tau^*} \mathrm{d}S \;+\; \int_S \left[\frac{F_r + F_m}{r^2 \left(1 - M_r\right)^2}\right]_{\tau^*} \mathrm{d}S \\
& +\; \frac{1}{c_0} \int_S \left[\frac{F_r \left(r M_r \dot{+} c_0 M_r - C_0 M^2\right)}{r^2 \left(1 - M_r\right)^2}\right]_{\tau^*} \mathrm{d}S \\
& +\; \int_S \left[\frac{Q_r \left(r M_r \dot{+} c_0 M_r - c_0 M^2\right)}{r^2 \left(1 - M_r\right)^3}\right]_{\tau^*} \mathrm{d}S.
\end{aligned}
\tag{2.5}
$$

2.2 Computational Aeroacoustics

2.2.1 Introduction

Computational methods have advanced the evolution of modern engineering analysis techniques; and aeroacoustics is not an exception. Much of the advancement in acoustic analysis has arisen, in response to the availability of large computational resources. So far computational fluid dynamics has been the main tool in the development of new design in aeronautics sector, advances in both numerical techniques and increased computing power of computers being the key. The trend to apply powerful and effective Computational fluid dynamics (CFD) methods is on the increase, due to the complexity of the flow physics engineers have to deal with in aeronautics. Computational aeroacustics (CAA) is different from CFD in the sense that it involves the development of schemes to approximate spatial and temporal derivatives in a way that preserves the physics of wave propagation, a phenomenon of little significance in typical aerodynamic computations because aerodynamic noise is a fractional by-product of fluid flows. Also generally, aerodynamic problems can sometimes be modelled as time independent where as aeroacoustics problems are, by its very nature, time dependent. Generally CAA includes a number of constituents, e.g. nearfield flow and source modelling, integral formulations, etc. For source modelling, CAA involves solving both the

aerodynamic and aeroacoustic problems simultaneously and is based on the solution of the fluid motion equations by classical field methods (e.g. finite volume, finite element, finite difference). In other words CAA attempts to resolve directly wave propagation to the far-field. Because of the classical field methods employed in solving fluid equations in CAA, it requires large computational resources in order to avoid excessive dissipation in solution. The requirement in computational resources increases as the observer distance is increased. For example, due to this drawback, an acceptable solution could only be obtained at a reasonable cost for observers at a distance of about 3 times the rotor radius in the case of helicopter noise [13](this figure is based on present computational capability available). In practical situations, however, the observer distance usually required is about two to three orders of magnitude greater than the wing chord. Therefore, the problem of direct numerical simulation of airframe noise is still beyond the capabilities of CAA based on currently available computing power.

In attempting to simulate noise problems, possible problems exist due to error accumulation in numerical methods. Numerical schemes approximate the non-dispersive, non-dissipative systems of governing equations through discretisation, which has numerical dissipation and dispersion, introducing errors that may significantly affect the accuracy of the calculation. This has been the main challenge in aeroacoustics since the computational methods were firstly employed. When the acoustic waves are part of the source mechanisms, as in cases involving acoustic/flow feedback, numerical dispersion is the most harmful in these situations because it corrupts the phase information of the waves affecting the interaction between flow and sound [14]. This is also the case when there is flow-acoustic interaction. Minimisation of dispersion and dissipation errors is important when numerical techniques such as finite difference and finite element methods are used for spatial discretization in solving propagation problems, especially when the propagation length is a distance of many wavelengths. This causes the dissipation to accumulate over the propagation length resulting in significant changes in wave amplitude. It is therefore desirable to use low dissipation schemes.

Generally central differencing is preferred in CAA applications. With reference to integral formulations used in aeroacoustics, numerical dispersion has not been a matter of great concern. This is because, firstly, airframe noise is important in approach condition (i.e. when Mach number is typically 0.2-0.3) hence compressibility is not important. This means that the simulation of flow can be performed independently of acoustic fields leading to no degrading effects in the farfield propagation due to interactions between the two. Secondly, and most importantly, the

numerical dispersion and dissipation issue may be avoided when using unsteady CFD and an integral surface solutions, e.g. the FW-H equation [14] because the propagation of the acoustic waves to far-field is handled by an integral formulation that exactly preserves the non-dispersive and non-dissipative nature of the sound waves; no numerical discretisation is involved in the formulation and the wave characteristics are exactly computed. However, increases in accuracy requirements and the development of aircraft with fewer localized noise sources will drive the need for improved dispersion and dissipation characteristics. Hence the desire for increased accuracy will always be present. Kurbatskii *et al.* [15] presented a collective overview of the numerical tools currently available in aeroacoustic research and on going developments. Subsequent sections below discuss a few of these popular low dispersion, higher order schemes available currently.

2.2.2 Dispersion-relation-preserving (DRP) scheme

Tam and Webb [16] proposed a higher order finite difference scheme (widely known as Dispersion-Relation- Perserving (DRP) scheme) to reduce dispersion so that the wave number of original differential equations are replicated by the solution of finite difference equation. The numerical solution of a higher order finite difference scheme will have the same number of wave modes as the original differential equation if both systems have the same dispersion relations. They found that it was possible to achieve the same dispersion relation between the numerical and the exact solution as long as the points-per-wavelength greater than four was maintained for the system under consideration. But there will always be the truncation error depending on the order of the discretization scheme. The derivation of the method uses Fourier-Laplace transforms rather than the usual truncated Taylor series. The use of Fourier analysis offers several flexibility including stability investigations, specification of acceptable errors from numerical calculations, etc. The authors used asymptotic solutions to develop the radiation and outflow boundary conditions for the DRP scheme. The transform method allows one to construct the asymptotic solution of the finite difference equations. The study shows the superior performance of the proposed higher order explicit finite difference scheme over standard finite difference schemes. The numerical study, however, was performed unidiagonally instead of multidiagonally. It, however, requires large number of stencils (i.e. seven stencils for the fourth order spatial accuracy [16]).

2.2.3   Compact scheme

Kim and Lee [17] proposed a weighted optimization technique for the optimization of compact finite difference scheme. The DRP scheme of Tam and Webb explained above was developed to minimise the dispersive errors in wave number domain, however it was a unidiagonal scheme. Therefore, the work of Kim and Lee is essentially an extension of Tam's unidiagonal DRP scheme to multidiagonal (tridiagonal and pentadiagonal) compact scheme with high-order and high resolution. It is obvious that the overall error of a numerical computation is determined by both the resolution and the order of truncation; and actual error characteristics of the compact schemes are dependent on their multidiagonality (i.e. usually expansion from unidiagonality to multidiagonality results in improved resolution and truncation order). They found that the optimized sixth-order tridiagonal and the optimized fourth-order pentadiagonal scheme performed the best of all. The tridiagonal scheme would be especially interesting as it is more computationally efficient than the pentadiagonal one (i.e. it needs only tridiagonal matrix solver). This scheme, however, is limited to problems with smooth solutions. For this to be applicable to highly discontinuous solutions, it must be developed to be able to detect the presence of discontinuities and noise oscillations.

2.2.4   Prefactored compact scheme

Hixon [18] proposed small stencil compact scheme of prefactored type. The main feature of the method is that the tridiagonal matrices in higher order compact schemes, which otherwise require LU-decomposition technique, is reduced to two independent upper and lower bidiagonal matrices. This then can be solved in parallel. Also the stencil size is reduced from five points to three for the sixth order accuracy; and due to smaller stencil size, only one boundary stencil is required instead of two. Hixon also showed that the stability and accuracy of the proposed scheme was much more dependent on the performance of the boundary stencils than in the case of equivalent explicit schemes. This is because the error from the boundary stencil derivatives can propagate many points into the computational domain.

2.2.5   Optimized prefactored compact scheme

Ashcroft and Zhang [19] proposed new optimized prefactored compact schemes in an effort to reduce dispersion and dissipation errors in aeroacoustic problems. This, in a sense, was the improved extension to the scheme developed by Hixon [18]. This method used Fourier analysis similar to the one used by Kim *et al.* [17] rather than Taylor series expansion used by Hixon and performs optimization to achieve the best possible accuracy and range factor. An obvious benefit in using Fourier series is that it allows one to optimize the dispersive scheme by quantifying the dispersive errors. This method also used a weighting function and optimization range factor. The study shows a reduction in grid resolution requirements when compared to Tam's DRP and Hixon's prefactored compact schemes. Although the explicit DRP scheme requires relatively less computational power than optimized prefactored compact schemes of Ashcroft and Zhang, the gain in resolution and accuracy in the latter outstrips the computational overhead. It was also concluded that a fourth-order three point scheme provided the best overall performance in terms of resolution versus computational cost.

At this point it is necessary to point out that the problems in aeroacoustics are, by its very nature, time dependent. Hence just ensuring high spatial accuracy in isolation does not ensure good result in aeroacoustic simulations. DeBonis *et al.* [20] studied the consequences of disparate temporal and spatial descritizations. Their computational study found that for schemes with lower order time stepping, the truncation error caused by time stepping dominated the solution reducing the overall error of the scheme to the order of time stepping and eliminating the benefit gained from higher-order spatial discretization. The study included Gottlied-Turkel 2-4 predictor-corrector scheme and two stage Runge-Kutta schemes (4-4 and 4-6). The Gottlied-Turkel method is fourth order accurate in space and second order accurate in time. Reducing the time step was found to increase the order of accuracy but with an increase to computational cost. The Runge-Kutta 4-4 scheme was found to perform best of all computationally.

2.2.6   Patched grid methods

Computational analysis of complex configurations using structured grids almost always (apart from geometrically simple cases) requires multiple blocks of grids. Even so, one-to-one matching at block interface while generating multi-block grids can cause significant difficulty depending on the complexity of the configuration.

Also an attempt to create a structured grid for a complex geometry causes highly skewed cells which, in turn, results in inaccurate calculations. Another factor which can cause major problems in generating a structured grid is the necessity to cluster grid points in regions where the flow variables and their gradients change rapidly. These issues are relevant to this research project as the configuration being considered is complex and a structured grid is used in the project.

The grid generation issue mentioned above can be improved by the use of zonal or patched grid method. The patched grid method allows one to generate grid in each block independently i.e. it does not require one-to-one matching. Then inter-block communication is established by using a suitable interpolation at the block interface. Rai [21, 22] proposed a patched grid algorithm for Euler equations based on linear interpolation at the inter-block interface. Conservation is ensured at the grid interface using one sided flux interpolation at the boundary. The interface condition for one subdomain is defined from the conservative variables while for the adjacent subdomain the interface condition is defined from the numerical flux. Rai's method of achieving conservation at the boundary can be difficult to achieve and implement in higher order schemes. Lerat and Wu [23] proposed a stable and conservative patched grid algorithm for compressible flow. They demonstrated that their scheme was able to predict discontinuities in high speed flow. They also pointed out that they were unable to achieve general stability for Rai's scheme [21, 22]. But Lerat and Wu's scheme is conservative and stable for dissipative difference schemes. Similarly Benkenida *et al.* [24] proposed splitting and dividing approach similar to the work of Lerat and Wu [23] to maintain the conservation at the block interfaces. The main issue in patched grid methods is achieving conservation and overall stability of the schemes. It will not be a issue in case of dissipative difference schemes as that of Lerat and Wu [23]. But achieving stability for high order accurate, non-dissipative, centered schemes (i.e. compact schemes) can be impossible by employing simple interpolation at the boundary.

2.3 Far Field Noise Prediction

2.3.1 Introduction

Sound waves radiated by almost all of the practical sound sources are non-planar. Hence the acoustic pressure and velocity at points near most sources are not in phase. Also values of sound levels measured close to a source normally show appre-

ciable variations with position. The near-field of a sound source generally extends for a distance equal to one or two characteristic source dimension and is a function of the sound frequency of interest, the dimension of the source and the relative phase of the radiating surface of the source. Whereas away from the source, acoustic pressure and velocity become simply related as in plane waves. This region is generally known as the far-field of the source. Acoustic analogies (first pioneered by Lighthill and extended by others [8, 11, 2]) use the unsteady flow informations on the near-field, to predict the far-field noise. Some of these techniques will be explained in subsequent sections that immediately follow. Acoustic analogies are reformulations of governing fluid flow equations (compressible Navier-Stokes equations). In this method, the Navier-Stokes equations are rearranged in the form of an inhomogeneous wave equation with source terms on the right hand side. Source terms are then made independent of the fluctuating acoustic variables with some assumptions. Such formulation represents a linear wave problem at rest with equivalent acoustic sources (monopoles, dipoles and quadrupoles) derived from an unsteady flow. An aeroacoustic problem (based on instability in fluid flow), hence, can essentially be converted into a problem of classical acoustics. This is the reason why the formulations based on this approach are widely known as acoustic analogies. One of the interesting aspects of integral methods is that the required computational time is independent of the observer distance. However increasing the observer distance means increased amount of analysis data, hence high storage requirement. Integral methods require knowledge of the aerodynamic flow field around the body surface which then permits one to evaluate the acoustic pressures at any point of the field by executing a certain number of integrals. Typical aerodynamic noise calculation therefore is performed in two steps, popularly known as hybrid method. In the first step, CFD calculations are performed to retrieve the necessary flowfield variables demanded by the integral formulations in the second step. Then an integral formulation is applied to propagate the disturbances to the farfield. It is necessary to comment on the Tam's [25] finding that the acoustic analogy should not, in anyway, be taken as the absolute answer by acoustic researchers. Tam pointed out that the acoustic analogy fails to identify correct acoustic sources in turbulent flows, and may not be a suitable tool for noise problems where large turbulent structures and fine-scale turbulence define radiated sound fields (e.g. high Mach number flow, jet noise problems etc). This is not always true. There should be no dispute in the fact that acoustic analogy can be used to predict the radiated noise as long as nature of turbulence is known in sufficient details. Hence it is not acoustic analogy which fails to identify the correct acoustic sources in turbulent flows, it is the choice of turbulence model

which determines the accuracy of the noise prediction. As there is no absolute answer in the choice of turbulence model which depends on individual problem, so is in aeroacoustic simulations.

2.3.2 Ffowcs Williams-Hawkings (FW-H) formulation

This formulation is based on an exact rearrangement of the continuity equation and the Navier-Stokes equations into the form of an inhomogeneous wave equation with two surface source terms (monopole and dipole) and a volume source term (quadrupole) [2]. This formulation embodies the most general form of the acoustic analogy. It permits the use of both impenetrable walls as well as permeable interior surfaces off the wall as integration surfaces. Therefore it is able to deal with much broader classes of acoustic problems than that by Curle's integral formulation [26]. It is linear when the quadrupole distribution is neglected; which is valid in the case of many subsonic applications; taking into account of quadrupole source terms requires substantially more computational resources due to the need for volume integration. It is, however, necessary to take into account the volume source term while calculating noise radiated in high speed flow condition (e.g. transonic and supersonic flow conditions). Another advantage is that the three source terms present in this method each have physical meaning. This was demonstrated in the study by Brentner [27] in the case of helicopter rotor noise. The monopole source term in Eq. 2.4 represents the thickness noise and is determined completely by the geometry and the kinematics of the body. The second term (dipole source) on the other hand represents the loading noise and is generated by the forces that act on the fluid as a result of the presence of the body (i.e. rotor in this case). Finally the volumetric source term represented by Lighthill's stress tensor accounts for the nonlinear effects, e.g. nonlinear wave propagation and steepening; variations in the local speed of sound; and the noise generated by shocks, vorticity, and turbulence in the flow field. This is helpful in understanding the noise generation mechanism and designing quieter airframe components. Olson *et al.* [28] and Singer *et al.* [29] used this formulation to simulate noise propagation.

2.3.3 Kirchhoff's formulation

This is another integral formulation which, unlike the FW-H formulation, does not require volume integration because it has only a surface source term. This is the reason why this method has been particularly popular in past in the prediction

of transonic noise generated by advancing rotor tip of helicopters. To adapt the FW-H scheme in this situation would be computationally expensive, the reason being the quadrupole source term is no longer negligible thus requiring a computationally demanding volume integration. However, Kirchhoff's formulation requires the integration surface to be chosen in the linear flow region (i.e. away from the region where significant velocity gradient exists), but the linear region itself may not be well defined and is problem dependent. It is, therefore, necessary to specify the integration surface well away from the body surfaces (e.g. aerofoil surfaces). Specification of integration surface well away from the body surface (at least one aerofoil chord away from the wall surface in case of high-lift noise simulation) has negative effects as CFD solutions may not be resolved away from the wall surfaces. Hence the placement of the Kirchhoff's integration surface is a compromise. Due to this short fall, Manoha *et al.* [30] had to use discritized linearised Euler equations (LEE) governing acoustic propagation in the non-linear region (i.e. the region between wall surface and the Kirchoff surface) before using Kirchhoff's formulation to propagate the acoustic disturbances to the farfield. Hence Manoha's study involved a three step procedure (See Section 2.4.1). The use of LEE, however, increases the computational cost significantly since the propagation domain must be meshed with an adequate resolution with respect to the smallest acoustic wavelength, and also because finite difference higher order schemes are needed to ensure numerical accuracy and low dispersion of the propagation of acoustic waves. However, the domain where LEE is used is strictly limited to the area of significant velocity gradients, normally small in most airframe noise problems so that a viable solution can be obtained. Although this avoids the evaluation of volume integral, it requires knowledge of derivative of pressure in the direction normal to the surface. This can impose difficulty especially when there are discontinuities on the surface. In the case of the FW-H equation it requires values of pressure, density and the flow velocity perturbations, which are available from CFD solutions.

2.3.4 FW-H vs Kirchhoff's formulation

Brentner *et al.* [31] investigated the FW-H and Kirchhoff formulation comparatively to address the superiority between the two in airframe noise prediction. The first clear advantage is that the FW-H formulation hints towards the insight into the acoustic field in that the predicted noise is explicitly separated into physical components, i.e., thickness, loading and quadrupole terms. Also FW-H method

can include non-linear effects of volume quadrupoles on its surface integral without having to perform volume integration if the usual assumption of impenetrable surface is relaxed. This can be achieved by lifting the integration surface to enclose all the intense volume quadrupole terms usually present near the body surface. The study of Singer *et al.* [29] found very different noise spectra for different integration surfaces employed. Kasper *et al.* [32] assessed the radiated noise from volumetric sources in case of a two-dimensional three-element aerofoil by comparing a permeable surface integration with the sum of solid body surface integration and a volume integral. Their study resulted in different spectra for body aligned integration surface and an off-body surface. Also the result of off body integration surface was in good agreement with the sum of the result of solid-body integration surface and volume integral[1]. This indicated that the volumetric sources were not negligible and the off body integration surface was found to take into account of the volumetric sources.

Ffowcs Williams has pointed out the several implications of the permeable surface ($f = 0$) in section 11.10 of reference [33]. The placement of the integration surface for the FW-H method is a matter of convenience as long as the quadrupole source term is utilized. Predicted acoustic pressure field by the Kirchhoff method can incur serious errors if the integration surface is placed in the non-linear region e.g. wake of an aerofoil. This was experienced in the work of Manoha *et al.* [30] in the case when the integration surface intersected the wake behind the trailing edge of a slat, the result was conflicting with the experiment. A final advantage of the FW-H approach is that it is relatively matured and has robust algorithms that have been validated for a variety of industrial problems today. Recently, Kim *et al.* [26] implemented FW-H formulation in Fluent,a general purpose commercial CFD code, for aeroacoustic analysis. This implementation accounts only for stationary integration surface yet allowing for permeable integration surfaces. It is based on advanced time formulation for better computational efficiency. The accuracy and suitability of the results from these general purpose commercial codes, however, are prohibitive mainly because they are implemented in a lower order scheme.

---

[1]This is the only research paper cited so far which evaluated volume integral and probably is the first research work to evaluate volume integral to date.

2.4   Slat Flow and Noise Research

2.4.1   Basic aerodynamic fields

The geometric and aerodynamic complexity of high-lift systems makes the understanding, and hence control of noise sources difficult. The velocity through the gap between the slat and the main element can be as high as twice the free stream value [34]. It has been found that reducing the gap reduces the noise, but reduced lift could be the consequence. Narrowing the gap chokes the pressure-side flow so that the cove region starts to behave as a plenum. Hence the key noise producing structures can not form or are attenuated. However, as the gap between the slat and the main element is made smaller, the slat wake begins to merge with the main element boundary layer, resulting in a flow layer called confluent boundary layer[2] [35]. The location of the starting point of confluence moves forward as the gap is decreased. The resulting confluence viscous layer will be thicker than the main element boundary layer alone, which increases the likelihood of the flow separation on the main element for increasing angle of attack [35]. Even if flow does not separate, an early confluence gives rise to enhanced mixing between the viscous wall layer of the main element and the slat wake. This mixing produces an increased momentum defect near the wall and an associated increase in displacement and momentum thickness over the main element. This has the effect of reducing the suction on the main element, and consequently lift is reduced. Thus even in the absence of the main element separation, lift is reduced as a consequence of confluence due to the associated outward streamline displacement effect.

Khorrami *et al.* [36] performed unsteady flow simulations of an energy efficient transport wing with high-lift devices deployed to explain the mechanism for vortex shedding. The study was performed with a fully turbulent mode employing a two equations (k-w) turbulence model. The computed result was found to display clearly the recirculating zone in the slat cove, the free shear layer originating from the slat cusp and acceleration of the flow through the gap between the slat and the main element. The existence of a vortex shedding at the slat trailing edge was also observed in the study. These unsteady features in the slat cove region are thought to be responsible for the slat noise generation mechanism which is explored in the next section. A generic noise generation mechanism due to a leading edge high lift device is shown in Figure 2.2.

---

[2]The mixing of a wake from an upstream body with the boundary layer on a downstream element is commonly referred to as a confluent boundary layer.

2.4.2 Noise generation

An aeroacoustic study of slats in a 3D high-lift system by Storms *et al.* [37] suggested that vortex shedding from the slat trailing edge is an important noise mechanism. Their study involved Strouhal frequency scaling based on slat trailing edge thickness and local slat gap velocity. But Strouhal number was found to vary with slat deflection and gap velocity indicating there must be a more complex phenomena rather than just the vortex shedding at the trailing edge. The study suggested that the slat noise could be a result of a feedback mechanism between vortex shedding and the Kelvin Helmholtz instability that develops in the slat cove. An investigation into slat noise production mechanisms by Olson *et al.* [28] indicates that the slat deflection angle has a controlling impact on the type of noise produced. It also points out that parameters other than the deflection angle alone determine the occurrence of tonal noise, and source strength and frequency are affected by gap and overhang setting.

Mendoza *et al.* [34] carried out detail aeroacoustic evaluation on a wing/slat model experimentally. The experimental set up consisted of a 2D airfoil with a leading edge slat. The test was conducted at large angle of attack (i.e. main element was aligned at geometric angle of 26 deg and 32 deg relative to the undisturbed flow) to compensate for the lack of lift typically generated by a main element and flap in high lift configurations. A number of slat acoustics phenomena were investigated. They found that reducing the gap between slat and main element resulted in reduced noise level at low frequency range. Another feature studied was the effect of varying the trailing edge bluntness. Thicker trailing edge resulted in a relatively large peak in the spectrum which increased in frequency as the Mach number was increased. However, at constant Mach number the low frequency spectrum was unchanged due to added bluntness and mid to high frequencies were affected only in the range where vortex shedding from the blunt trailing edge occurred. Their measured data and analysis showed that the key slat noise came as a result of trailing edge noise from both the suction and pressure side of the slat. Slat noise is found to be composed of high frequency tonal components and a low frequency broadband part. Figure 2.3 shows a generic slat noise spectrum plotted against Strouhal number based on the slat chord.

Khorrami and Lockard [38] investigated the effect of the geometrical details in the slat noise by including a slat bulb and a slat seal in their computational study. Their study showed that the slat bulb did not have significant effect on the cove flow characteristics or noise generation. However, the addition of a blade seal to

that slat cusp altered the shear layer characteristics reducing the strength of the vortices growing in the layer. The longer blade seal also reduced the strength of shed vortices at the slat trailing edge. They found that the blade seal to reduce the broadband signal by $2 - 3$dB and significantly diminished the tonal component.

High Frequency Tonal Noise Singer *et al.* [29] performed highly resolved, time dependent RANS simulation of slat flow and noise. An acoustic analysis was then performed based on FW-H equation with input from the RANS calculations which showed the presence of vortex shedding from the trailing edge of the slat for the 30 deg slat deflection. This vortex shedding, however, virtually disappeared at 20 deg. The vortex shedding was asserted to contribute to the high frequency acoustical signal present on the slat noise spectra. The physical mechanism for this vortex shedding was not known at the time. Although several other studies showed the presence of a high acoustic peak at the 30 deg slat deflection in their study, no clear understanding of physics behind the underlying noise source had emerged [39, 40, 41] (two of these tests included 30 deg slat deflection).

Khorrami *et al.* [36] proposed the conjecture that the vortex shedding at somewhat blunt slat trailing edge was the mechanism responsible for the hump at high frequency. In the work of Khorrami *et al.*, while performing unsteady aerodynamic simulations in 3D, two different computational domains with two different values of the trailing edge thickness (0.07 and 0.09 percent of the mean chord i.e. 0.39mm and 0.5mm) were generated. Another interesting feature of this simulation was the use of patched[3] multiple-blocks in grid generation. It was proposed that the shear layer along with the recirculation zone is an important source of flow unsteadiness and noise generation especially in the case of the low frequency spectrum. The result also confirms the existence of a vortex shedding process at the trailing edge. At the 30 deg slat deflection, the wake is deflected slightly upward due to a fast moving gap flow and the presence of thicker boundary layer on upper surface. Near to the trailing edge there is a small region of reversed flow in the wake centre line, hence suggesting the existence of absolute instabilities causing the vortex shedding (i.e. the wake is almost symmetrical, hence absolute instabilities are likely to exist). But in the case of 20 deg slat deflection, the wake is asymmetrical due to the more intense flow through the gap, causing the disappearance of vortex shedding.

---

[3]Patching involves reducing the number of mesh points in one or two directions across a common interface shared by two adjacent grid blocks resulting in reduction in total no. of grid points and allowing the fine clustering of grids in region of interest e.g.slat cove, slat trailing edge wake, etc

In another study, Khorrami *et al.* [42] studied the noise generation mechanism of a slat at varying angles of attack. It was found that at high angles of attack a high frequency tone exists but this tone disappears at reduced angles of attack. An investigation of physical mechanisms behind this broadband behaviour concluded that vortex shedding at the slat trailing edge was responsible for this high amplitude tonal sound. The computational simulation of the vortex shedding mechanism becomes challenging because the real slat trailing edges have finite thickness and to accurately simulate the mechanism of vortex shedding, it is important to capture the wake accurately. To capture the wake accurately, a dense grid is required at the trailing edge. Of particular significance is the reflection of the waves at the leading edge of the main element which results in a distinct interference pattern across the gap and the cove area. The computational study of Khorrami also agreed well with the measured trends of the NASA experimental results [39]. At lower angles of attack, no high amplitude tone was found to be present in experiment and no vortex shedding was observed in computational solution confirming the trend. Also a reduction in amplitude and a shift to the lower shedding frequency for lowering Reynolds number flows in the computational simulation agreed with the experimental trend.

Tam and Pastouchenko [43] proposed that the frequency of vortex shedding at the slat trailing edge is set by a feedback loop. A vortex is first shed at the slat trailing edge, which acts as an acoustic source. The acoustic waves then travel through the slat gap while being convected with the flow. They are reflected from the main-element and strike the slat trailing edge. This results in another vortex being shed. This process repeats, setting up the vortex shedding frequency. In their model, shear layer starts with nearly zero thickness as Euler equations are solved upstream of the slat trailing edge and the trailing edge thickness is also assumed zero. Thus, in the viscinity of the slat trailing edge, there are neither any incoming boundary layers nor any trailing edge thickness. Thus, it can be assumed that such a negligibly thin shear layer from an infinitely thin splitter plate (i.e. trailing edge is assumed to have zero thickness) would be able to support any frequency associated with Tam and Pastouchenko [43] acoustic model (i.e. the resonance tone should occur at any frequency). But this acoustic model can not explain all the features observed in experiments [39, 40, 41] (i.e. in the experimental work of Storms*et al.* [39], no vortex shedding was observed in the case of 26 deg slat deflection. Similarly, there was no vortex shedding in case of 20 deg slay deflection in the experimental work of Khorrami *et al.* [36].).

The physical mechanism of the generation of high frequency tonal noise was studied

in detail by Agarwal and Morris [44]. They proposed a mechanism in the form
of an aeroacoustic whistle to explain these high frequency tones and they pointed
out that the bluntness of the slat trailing edge, finite thickness of slat boundary
layer, along with the gap between slat and the main element of a wing constituted
to aeroacoustic whistle. The whistling mechanism can be simply explained with
the aid of Figure 2.4. Acoustic waves radiated from the slat trailing edge strike
the main element and reflect back towards the slat trailing edge. Only rays which
are pointing directly beneath the slat trailing edge strike it and reflect back off
again. Hence this cycle repeats itself indefinitely. When all these round trip waves
are in phase, then resonance occurs and the resonance frequency is given by,

$$f_r = n\frac{\sqrt{a^2 - u^2}}{2d}. \tag{2.6}$$

Where n = 1,2,3,....

In the above equation, a and u are speed of sound and the magnitude of mean flow
through the gap between the slat and the main wing respectively. Aeroacoustic
whistling occurs when the vortex shedding frequency is equal to the resonance
frequency calculated above. The frequency f_r calculated above is also known as
the normal or natural frequency of the gap. Experimental results from NASA
have verified this aeroacoustic whistle mechanism for a range of angles of attack.
At a 30 deg slat deflection, the calculated transverse resonance frequency and the
vortex shedding frequency were found to satisfy the whistling condition. Whereas
in case of a 20 deg slat deflection, the transverse resonance frequency was found
to be slightly higher than that for the 30 deg case (as the mean velocity through
the gap is smaller). The vortex shedding frequency is expected to be smaller than
that for the 30 deg case because the slat is more aerodynamically loaded in the
former case leading to thicker boundary layer and thicker wake than the latter.
This leads to lower vortex shedding frequency than that of former. Increasing the
main element angle of attack has the same effect as decreasing the slat deflection
from the stand point of global aerodynamics. This immediately suggests that the
whistling condition is not satisfied this time. So no high amplitude tone occurs in
this case. This was also the case in the experiment. Also the effect of variation
of Mach number was studied. This resulted in increase in the frequency of the
observed tone. Agarwal and Morris explained that increase in Mach number leads
to thinner boundary layer thickness which in turn implies a thinner wake leading to
higher vortex shedding frequency. He also studied the effect of varying Reynolds
number. A downshift in the tone frequency was observed. This is because a

reduction in Reynolds number thickens the boundary layer and hence the wake leading to reduction in both gap resonance and vortex shedding frequency.

In another study, Takeda *et al.* [45] concluded that the presence of an acoustic feedback mechanism was necessary for cut-on of the slat tones to occur, however, it may not be strong enough to regulate vortex shedding in the presence of a finite trailing edge. They found that changing the trailing edge thickness caused a change in frequency, although, this does not scale as a function of edge thickness exactly, as the Strouhal number was seen to increase with thickness.

Low Frequency Broadband Noise   Although it was found that the high amplitude tonal sound disappears at low frequencies, the low frequency broad band noise increases with decreasing angle of attack. Experimental study has revealed that strong spanwise vortices are present in the slat's wake and these vortices are thought to originate at the slat cove region and then are pumped through the gap. But as the angle of attack increases, the unsteadiness in the cove decreases, thus, reducing the number of vortices responsible for low frequency noise significantly. Khorrami *et al.* [46] studied the contribution of shear layer to the low frequency part of the total spectra computationally and concluded that amplified perturbations in the shear layer are responsible for the low frequency broad band noise. Initially they performed a study of free shear layer which originated at the slat cusp using fully turbulent calculations to get a better idea about the oscillating flow present in the slat-clove region. The flow was simulated without any forcing mechanisms for the oscillating clove flow field because the shear layer itself is a good amplifier of perturbations. The results, however, showed that the initial perturbations present were damped out by numerical dissipation after a few periods. The flow was solved as fully turbulent, and the turbulent flow computations are diffusive due to the production term on the turbulence models. Later a forcing mechanism was applied near the cusp to maintain the instability mode in free shear layer. Simulations of forced shear layer resulted in sustained oscillatory mode by the free shear layer. The result shows the continuous rolling up of the shear layer and forming of the discrete vortices as they approach the reattachment point on the cove surface. The shear layer is good in amplifying initial perturbations that grow rapidly. The diffusive nature of fully turbulent calculation, however, results in dying out of the discrete vortices which were generated in the cove region. This disallows a proper development of the cove flow field which also means the vortices which otherwise will have escaped through gap will not do so in this case. This also produces the reduced acoustic signature than in the real case. Khorrami *et*

al. [47] argued that the flow field in the cove region was not entirely turbulent but it was unsteady quasi-laminar and hence they studied cove flow using laminar formulation in the cove region. No forcing mechanism was used in this case and the results obtained were dramatic. The laminar calculation on the cove region produced a highly unsteady flow field where there was shear layer oscillation. The roll-up and the formation of discrete vortices were also clearly observed in the cove region. The assumption is probably a valid one because the Reynolds number at slat cove region will be significantly small for the flow to be fully turbulent. The justification of their conjecture also answers the speculation of earlier researches mentioned above [48, 37, 29]. It is thought that this component of noise will be the most important in the study of slat track noise because the tracks are present in the cove region.

Terracol *et al.* [49] performed simulations of the turbulent 3D unsteady flow inside a slat cove of a high-lift wing system using a zonal hybrid RANS/LES approach. The first part of the simulation was performed to highlight the several unsteady flow features present in the flowfield which were associated to aerodynamic noise emission. This information was then fed to a CFD/CAA coupled scheme. The work essentially coupled an unsteady CFD zone where Navier-Stokes equations were solved (as mentioned above) with a CAA propagation zone; the sound prop-agation in the zone through an inhomogeneous mean flow was simulated by re-solving the Euler equation in the perturbed form. The method was found to be computationally efficient and was able to capture vortex shedding at the trailing edge. The method divides the flowfield into different domains in which specific physical mechanisms are simulated using the most adequate formulation with a cost effective discretization strategy.

2.4.3   Slat track flow and noise

An experimental study of a 3D geometry of a multi-element wing by Berkman *et al.* [50] found that spanwise variation of flow properties was pronounced in the flap area (i.e. they used a part span flap and full span slat. The flow variation due to flapside effect was found to be effective only locally) and it had no influence on the flow upstream of the main element (i.e. slat flow). Flow around the slat, hence, was essentially 2D. But the part-span flap changed the circulation around the wing thus increasing the loading on the slat. This will at least allow one to perform the computational study of a single track in the gap between the slat and the main element to represent the noise generation mechanisms of all the slat

tracks since essentially a 2D flow can be assumed to exist in the slat region. This is, however, only valid only for a straight wing. In case of a swept wing, the cove flow field will no longer be 2D. The cove vortex will vary in the spanwise direction, with phenomena called vortex stretching in third-dimension [51]. Interaction of these vortices with the slat tracks is thought to be an important contributor in the slat track noise.

An experimental study performed by Dobrzynski *et al.* [48] on a 1 : 10 scale high-lift wing with deployed high-lift devices included the investigation of the effect of slat tracks on the overall noise spectrum. The study revealed that the noise levels from the slat tracks were higher compared to a clean configuration by about 8dB in the frequency range tested (2kHz to 40kHz). The dominance of slat track noise is not surprising since the slat tracks are installed perpendicular to the wing leading edge for mechanical simplicity which hence causes additional flow separations as a result of oblique flow incidence. Vortex shedding from these slat tracks cannot totally be eliminated, however, such detrimental effects can be minimised if slat tracks are streamlined in shape and mounted aligning with the flow direction. Noise reduction benefit was demonstrated by Dobrzynski *et al.* in their experimental study by installing a slat track aligned in flow direction. Their study also indicated the slat noise is mainly a composition of trailing edge noise and the noise originating from the convection of turbulent eddies in the slat flow. Reichenberger [52] studied the various aspects of slat track noise and the techniques to reduce it. The study examined the use of a slat track fairing, aeroacoustic cover for the track opening in form of a shutter and a combination of fairing and a rubber band as shown in Figures 2.5, 2.6 and 2.7. These design modifications have been found to offer the slat track noise reduction. The experimental works [48, 52] have pointed out the significance of slat tracks on leading edge slat noise and the potential noise reduction methods [52]. A work on noise reduction aspects, however, requires a good knowledge of the source which causes the noise. The starting point of this project therefore is to perform computational simulation for the slat track geometry to understand the source of noise.
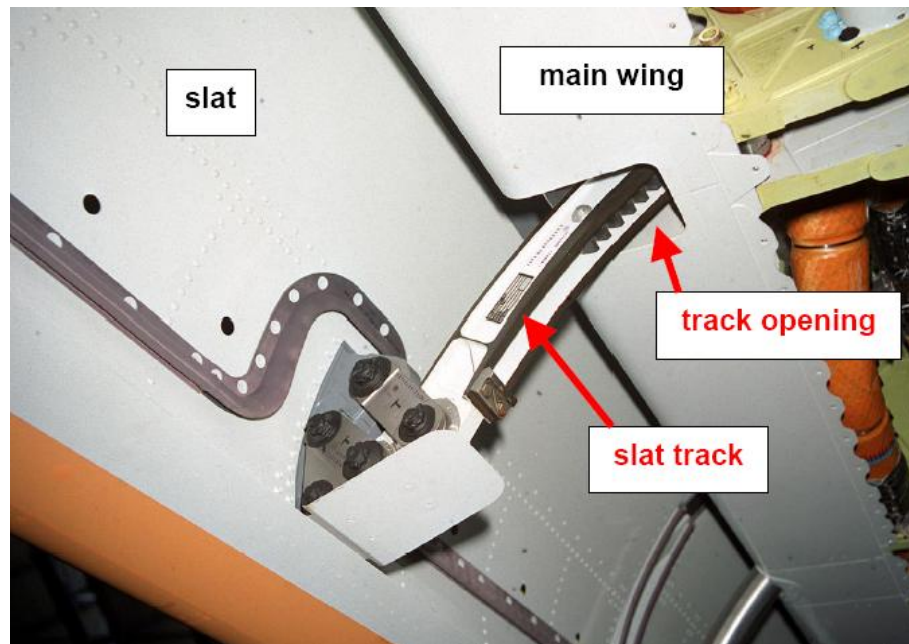
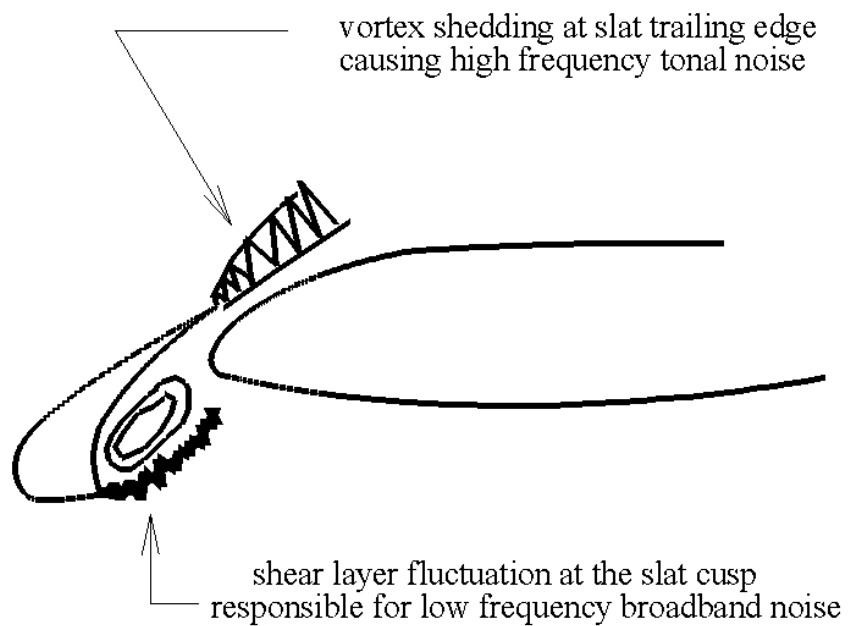FIGURE 2.1: Slat track on Airbus A340 outboard wing.

FIGURE 2.2: Schematic of a generic slat noise generation mechanism.

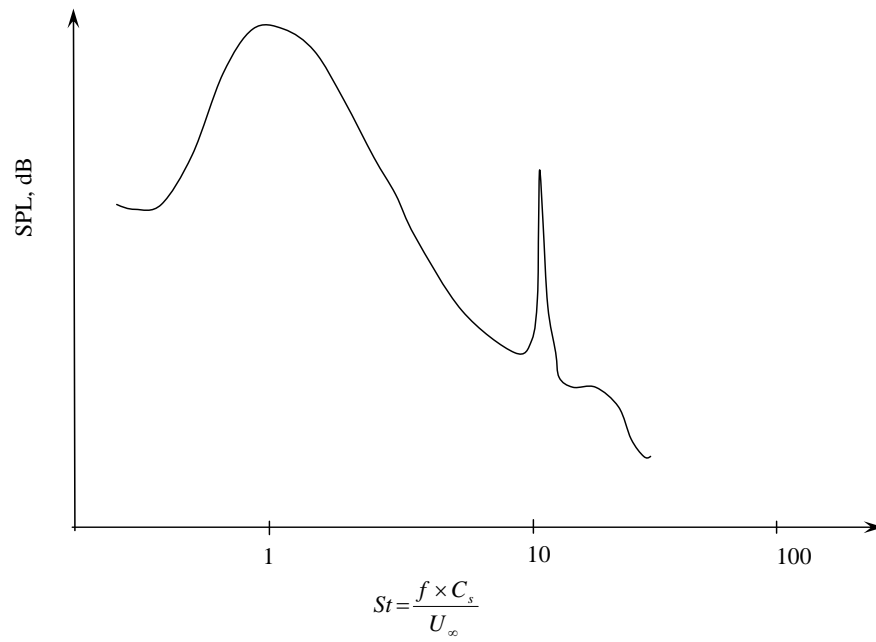$$St = \frac{f \times C_s}{U_\infty}$$

FIGURE 2.3: Schematic of generic slat noise spectrum based on Strouhal number.
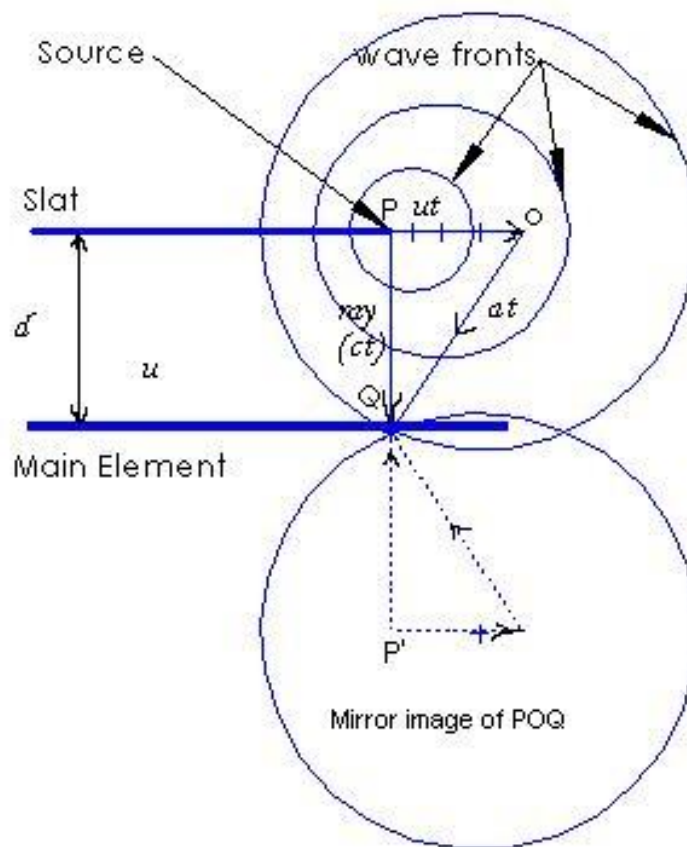
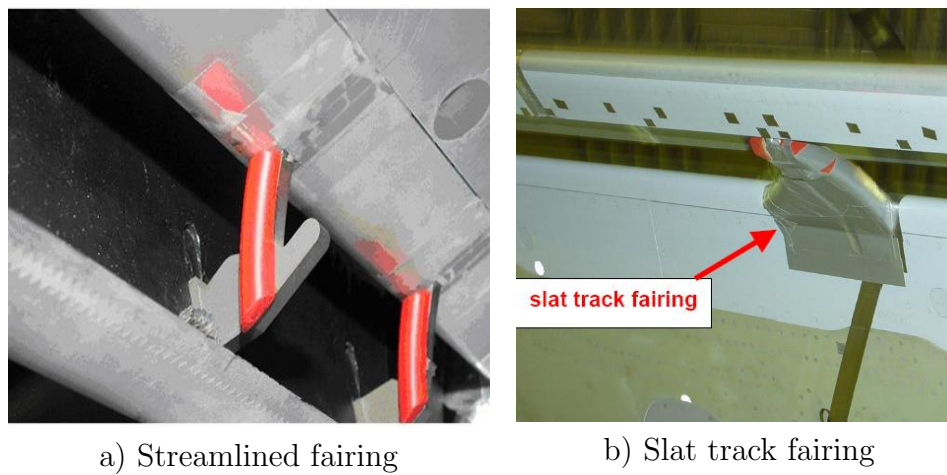FIGURE 2.4: Feedback process leading to resonance near the slat trailing edge.

a) Streamlined fairing b) Slat track fairing

FIGURE 2.5: Slat track fairing used in EC SILENCER project on Airbus A320.
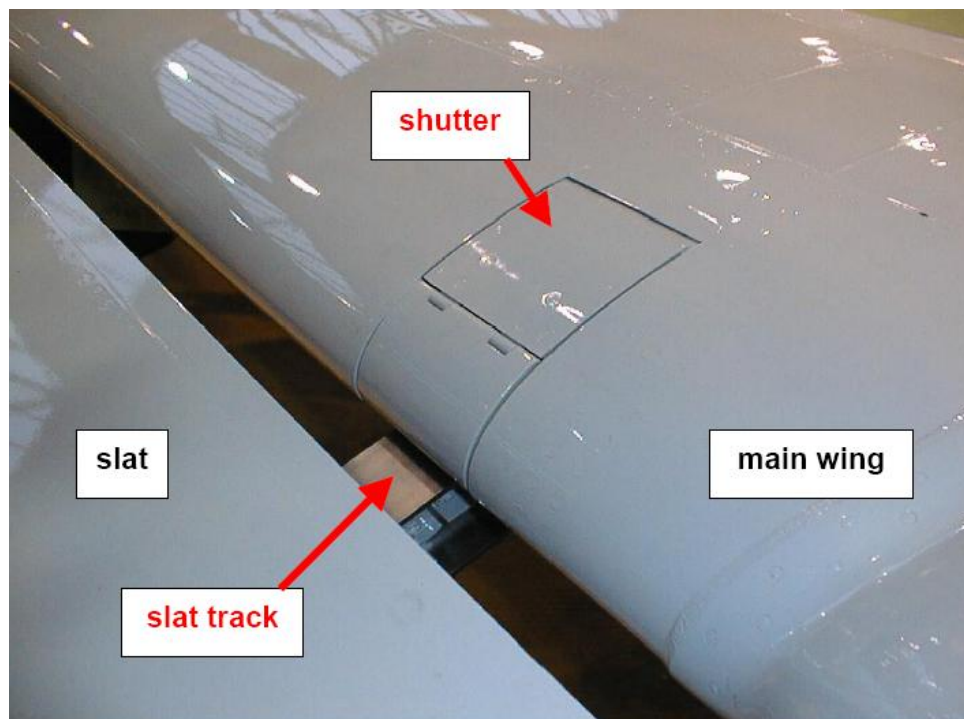
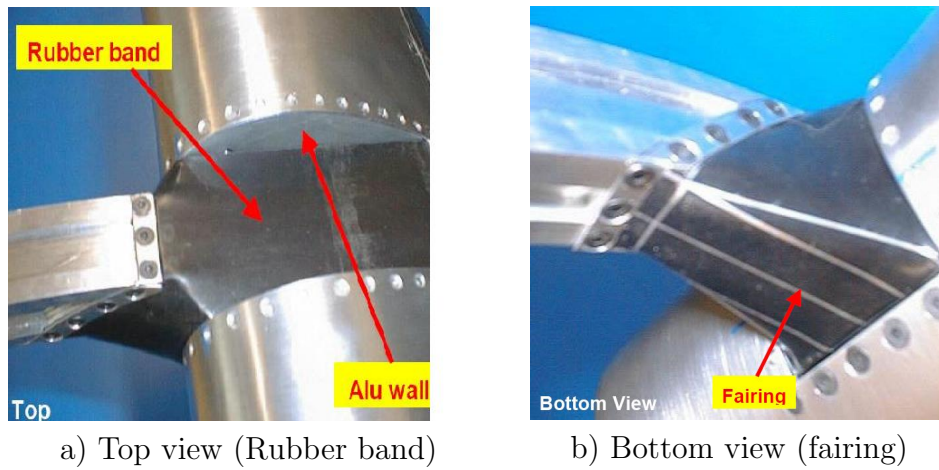FIGURE 2.6: Slat-track opening on Airbus A330 closed by a shutter.

a) Top view (Rubber band)   b) Bottom view (fairing)

FIGURE 2.7: Combination of a fairing and a rubber band.

Chapter 3

Computational Methodologies

The computational methodologies used in this project are outlined in this chapter. The chapter includes brief descriptions of the different solvers used and governing equations solved.

3.1   Introduction

The literature review indicated that a direct numerical simulation of the airframe noise was still beyond the capabilities of CAA based on currently available computing power. The use of near-field CFD computations coupled with solutions of FW-H equation is a practical alternative for the prediction of airframe noise. Hence the computational procedure adapted in this research is a two step method. Firstly, the governing equations of fluid dynamics are solved around chosen geometry using a computational grid. This provides the time-dependent flow information in the viscinity of the noise source. This flow results can be used as input to the FW-H solver to yield the acoustic information. This two-step method is illustrated in Figure 3.1.

Two different computational approaches are used to simulate the flow field and understand noise generation and propagation phenomena. Firstly the acoustic wave propagation phenomena are simulated using a propagation solver based on either the Linearized Euler Equations (LEE) or the Acoustic Perturbation Equations [53, 54]. Simulations with source modelling are performed in both 2D and 3D configurations to study the effect of slat tracks on sound wave propagation. The second approach involves using the Navier-Stokes simulations to better under-

stand the flow physics in the slat track region. A brief account of the computational solvers used are presented in the following sections.

3.2   The LEE and APE Solvers

Acoustic fields are defined by small perturbation components in an aerodynamic flow field. Propagation of these acoustic fields can be described by the Linearized Euler equations (LEE). An in-house near-field acoustic solver (SotonLEE) is used to perform computations for the propagation of acoustic waves in 2D and 3D geometries. The far-field propagation of the near-field LEE solution is computed using an efficient far-field prediction method based on the solution of FW-H equation. The LEE solver is used to study the propagation of an idealized source without mean flow. For the propagation study in presence of mean flow, APE (Acoustic Perturbation Equations) are used. They are modified forms of the LEE equations. The LEE equations also support the propagation of vorticity and entropy waves. Unlike the LEE, the APE equations do not support the propagation of vorticity mode. This section outlines the formulations of the governing equations used in the propagation solvers (LEE and APE).

3.2.1   Governing equations

The governing equations are based on the inviscid form of Navier-Stokes equations represented in conservative form:

$$
\begin{aligned}
\frac{\partial \rho}{\partial t} + \nabla.(\rho \mathbf{v}) &= 0. \\
\frac{\partial (\rho u)}{\partial t} + \nabla.(\rho u \mathbf{v}) + \frac{\partial p}{\partial x} &= 0. \\
\frac{\partial (\rho v)}{\partial t} + \nabla.(\rho v \mathbf{v}) + \frac{\partial p}{\partial y} &= 0. \\
\frac{\partial (\rho w)}{\partial t} + \nabla.(\rho w \mathbf{v}) + \frac{\partial p}{\partial z} &= 0. \\
\frac{\partial (\rho e)}{\partial t} + \nabla.(\rho e + p)\mathbf{v} &= 0.
\end{aligned}
\tag{3.1}
$$

For air as an ideal gas, $\rho e = \frac{p}{\gamma - 1} + \frac{1}{2}\rho(u^2 + v^2 + w^2)$. Which closes the system of equations above.

Assuming that the acoustic amplitudes are small compared to the background mean flow, the general system of LEE equations can be modelled by linearising the above set of governing equations about meanflow. Neglecting the second order terms, the LEE system of equation becomes:

$$\frac{\partial \rho^{'}}{\partial t} + \mathbf{V}_0.\nabla\rho^{'} + \mathbf{v}^{'}.\nabla\rho_0 + \rho_0\nabla.\mathbf{v}^{'} + \rho^{'}\nabla.\mathbf{V}_0 \;=\; 0.$$

$$\frac{\partial u^{'}}{\partial t} + \mathbf{V}_0.\nabla u^{'} + \mathbf{v}^{'}.\nabla U_0 + \frac{1}{\rho_0}\frac{\partial p^{'}}{\partial x} \;=\; 0.$$

$$\frac{\partial v^{'}}{\partial t} + \mathbf{V}_0.\nabla v^{'} + \mathbf{v}^{'}.\nabla V_0 + \frac{1}{\rho_0}\frac{\partial p^{'}}{\partial y} \;=\; 0.$$

$$\frac{\partial w^{'}}{\partial t} + \mathbf{V}_0.\nabla w^{'} + \mathbf{v}^{'}.\nabla W_0 + \frac{1}{\rho_0}\frac{\partial p^{'}}{\partial z} \;=\; 0.$$

$$\frac{\partial p^{'}}{\partial t} + \mathbf{V}_0.\nabla p^{'} + \mathbf{v}^{'}.\nabla p_0 + \gamma p_0\nabla.\mathbf{v}^{'} + \gamma p^{'}\nabla.\mathbf{V}_0 \;=\; 0. \qquad (3.2)$$

The set of equations in Eq. (3.2) is the basis of the in-house acoustic propagation solver SotonLEE developed by Richards [55]. Eq. (3.2) is expressed in cartesian coordinate. For the study of flow around complex geometries, the governing equations must be solved in orthogonal curvilinear coordinate system, also known as body-fitted coordinate system. This allows the complex geometry problem to be transformed into and simulated using a uniform computational domain, which is also easier to handle with finite difference schemes. The equations in the curvilinear are obtained after a transformation from the physical coordinate system to the computational coordinate system represented by Eq. (3.2).

$$\xi = \xi(x,y,z), \qquad \eta = \eta(x,y,z), \qquad \zeta = \zeta(x,y,z). \qquad (3.3)$$

Now the chain rule can be used to evaluate the spatial derivatives of the governing equation and hence the transformation metrics.

$$\frac{\partial}{\partial x} \;=\; \frac{\partial\xi}{\partial x}\frac{\partial}{\partial\xi} + \frac{\partial\eta}{\partial x}\frac{\partial}{\partial\eta} + \frac{\partial\zeta}{\partial x}\frac{\partial}{\partial\zeta}.$$

$$\frac{\partial}{\partial y} \;=\; \frac{\partial\xi}{\partial y}\frac{\partial}{\partial\xi} + \frac{\partial\eta}{\partial y}\frac{\partial}{\partial\eta} + \frac{\partial\zeta}{\partial y}\frac{\partial}{\partial\zeta}.$$

$$\frac{\partial}{\partial z} \;=\; \frac{\partial\xi}{\partial z}\frac{\partial}{\partial\xi} + \frac{\partial\eta}{\partial z}\frac{\partial}{\partial\eta} + \frac{\partial\zeta}{\partial z}\frac{\partial}{\partial\zeta}. \qquad (3.4)$$

Which then gives the transformation metrics as,

$$
\begin{aligned}
\xi_x = \frac{\partial \xi}{\partial x} &= J\left(\frac{\partial y}{\partial \eta}\frac{\partial z}{\partial \zeta} - \frac{\partial y}{\partial \zeta}\frac{\partial z}{\partial \eta}\right) \\
\xi_y = \frac{\partial \xi}{\partial y} &= J\left(\frac{\partial x}{\partial \zeta}\frac{\partial z}{\partial \eta} - \frac{\partial x}{\partial \eta}\frac{\partial z}{\partial \zeta}\right) \\
\xi_z = \frac{\partial \xi}{\partial z} &= J\left(\frac{\partial x}{\partial \eta}\frac{\partial y}{\partial \zeta} - \frac{\partial x}{\partial \zeta}\frac{\partial y}{\partial \eta}\right) \\
\eta_x = \frac{\partial \eta}{\partial x} &= J\left(\frac{\partial y}{\partial \zeta}\frac{\partial z}{\partial \xi} - \frac{\partial y}{\partial \xi}\frac{\partial z}{\partial \zeta}\right) \\
\eta_y = \frac{\partial \eta}{\partial y} &= J\left(\frac{\partial x}{\partial \xi}\frac{\partial z}{\partial \zeta} - \frac{\partial x}{\partial \zeta}\frac{\partial z}{\partial \xi}\right) \\
\eta_z = \frac{\partial \eta}{\partial z} &= J\left(\frac{\partial x}{\partial \zeta}\frac{\partial y}{\partial \xi} - \frac{\partial x}{\partial \xi}\frac{\partial y}{\partial \zeta}\right) \\
\zeta_x = \frac{\partial \zeta}{\partial x} &= J\left(\frac{\partial y}{\partial \xi}\frac{\partial z}{\partial \eta} - \frac{\partial y}{\partial \eta}\frac{\partial z}{\partial \xi}\right) \\
\zeta_y = \frac{\partial \zeta}{\partial y} &= J\left(\frac{\partial x}{\partial \eta}\frac{\partial z}{\partial \xi} - \frac{\partial x}{\partial \xi}\frac{\partial z}{\partial \eta}\right) \\
\zeta_z = \frac{\partial \zeta}{\partial z} &= J\left(\frac{\partial x}{\partial \xi}\frac{\partial y}{\partial \eta} - \frac{\partial x}{\partial \eta}\frac{\partial y}{\partial \xi}\right)
\end{aligned}
\tag{3.5}
$$

Where J is the transformation Jacobian which relates the geometrical properties of the physical domain to the uniform computational domain and is expressed as,

$$
J = \left[\frac{\partial x}{\partial \xi}\left(\frac{\partial y}{\partial \eta}\frac{\partial z}{\partial \zeta} - \frac{\partial y}{\partial \zeta}\frac{\partial z}{\partial \eta}\right) - \frac{\partial x}{\partial \eta}\left(\frac{\partial y}{\partial \xi}\frac{\partial z}{\partial \zeta} - \frac{\partial y}{\partial \zeta}\frac{\partial z}{\partial \xi}\right) + \frac{\partial x}{\partial \zeta}\left(\frac{\partial y}{\partial \xi}\frac{\partial z}{\partial \eta} - \frac{\partial y}{\partial \xi}\frac{\partial z}{\partial \eta}\right)\right]^{-1}.
\tag{3.6}
$$

The equations above are non-dimensionalised using the following reference values and solved in non-dimensionalised form.

$$
\rho^* = \frac{\rho}{\rho_\infty}, \quad \mathbf{v}^* = \frac{\mathbf{v}}{c_\infty}, \quad p^* = \frac{p}{\rho_\infty c_\infty^2}, \quad c^* = \frac{c}{c_\infty}, \quad \mathbf{x}^* = \frac{\mathbf{x}}{L}, \quad t^* = t/(L/c_\infty).
\tag{3.7}
$$

3.2.2 Modelled sources

Dipole and quadrupole sources are used to study the sound propagation phenomenon using the linearized solver. The source strength of these sources can be expressed as a combination of the source strengths of monopole source. A dipole source can be expressed as the combination of two equal and opposite monopoles. Similarly, a quadrupole source can be expressed by a combination of four monopole sources. The source strength of a monopole can be written as,

$$S(r) = A\omega e^{-Br^2} \sin \omega t. \tag{3.8}$$

Where A is the amplitude of the monopole source, ω the source frequency, B is an amplitude factor dependent on the grid interval size and r is the distance to the source point. A dipole strength can, thus, be written as,

$$S(r) = A\omega e^{-Br^2} \sin \omega t + A\omega e^{-Br^2} (-\sin \omega t). \tag{3.9}$$

The value of the amplitude A used was 2.5×10^{-3} in all the calculations. A schematic of these sources is shown in Figure 3.2.

3.2.3 APE equations

The LEE equations suffers from excited hydrodynamic instabilities when incorporated with CFD mean flows [53]. Hence to study the effects of mean flows in the source propagation, Acoustic perturbation equations (APE) are used. Ewert *et al.* [53] proposed source filtering method to derive a system of acoustic perturbation equations so that it is well suited for the simulation of solely acoustic modes. It differs from the linearized Euler equations as it does not possess the convection property for the vorticity perturbations. Details of source filtering technique is presented in Appendix .1. The full set of APE equations in 3D is given as:

$$\frac{\partial \rho^{'}}{\partial t} + \mathbf{V}_0.\nabla \rho^{'} + \mathbf{v}^{'}.\nabla \rho_0 + \rho_0 \nabla.\mathbf{v}^{'} + \rho^{'}\nabla.\mathbf{V}_0 = 0.$$

$$\frac{\partial u^{'}}{\partial t} + \frac{\partial \left(\mathbf{V}_0.\mathbf{v}^{'}\right)}{\partial x} + \frac{\gamma \rho^{'}}{\rho_0}\left(\mathbf{V}_0.\nabla\right)U_0 + \frac{1}{\rho_0}\frac{\partial p^{'}}{\partial x} = 0$$

$$\frac{\partial v^{'}}{\partial t} + \frac{\partial \left(\mathbf{V}_0.\mathbf{v}^{'}\right)}{\partial y} + \frac{\gamma \rho^{'}}{\rho_0}\left(\mathbf{V}_0.\nabla\right)V_0 + \frac{1}{\rho_0}\frac{\partial p^{'}}{\partial y} = 0$$

$$\frac{\partial w^{'}}{\partial t} + \frac{\partial \left(\mathbf{V}_0.\mathbf{v}^{'}\right)}{\partial z} + \frac{\gamma \rho^{'}}{\rho_0}\left(\mathbf{V}_0.\nabla\right)W_0 + \frac{1}{\rho_0}\frac{\partial p^{'}}{\partial z} = 0$$

$$\frac{\partial p^{'}}{\partial \mathrm{t}} + \mathbf{V}_0.\nabla p^{'} + \mathbf{v}^{'}.\nabla p_0 + \gamma p_0 \nabla.\mathbf{v}^{'} + \gamma p^{'}\nabla.\mathbf{V}_0 = 0. \qquad (3.10)$$

The solver SotonAPE is based on the set of equations in Eq. (3.10) and it was developed by Ma [56] in University of Southampton. SotonAPE was used in this research work to study the effects of background mean flows in noise propagation.

3.2.4 Numerical schemes

Conventional low-order CFD schemes used for aerodynamic computations cannot predict acoustic waves propagation accurately. Excessively fine grid systems are required for an acoustic propagation problem over a long distance. Even if the discretization scheme used is high-order, accurate prediction of acoustic wave is dependent on the dispersion and dissipation characteristics of the scheme. Hence a high-order discretization scheme with low dispersion and dissipation errors is desirable for an acoustic computation.

Spatial discretization Fourth order compact finite differencing based on the optimized prefactored compact scheme of Ashcroft and Zhang [19] is used in this research project for the calculation of spatial derivatives. This scheme is optimized for low dissipation and dispersion errors and is suitable especially for acoustic computations.

Temporal discretization To accurately predict the acoustic propagation problems both the temporal as well as spatial discretization schemes must have low dissipation and dispersion characteristics. Explicit low-storage Runge-Kutta scheme of Hu *et al.* [57] is used to advance the solution in time. This is a two-step alternating scheme optimized for low dissipation and dispersion errors.

3.3 Navier-Stokes Flow Solver

Finite volume based Navier-Stokes solver, FLUENT was used for the computation of background mean flows.

3.3.1 FLUENT Solver

FLUENT is a finite-volume solver and the temporal and spatial discretization schemes available in FLUENT provide at most second-order accuracy in space and time. It is widely used both in industrial CFD projects and academic research works. Many studies [26, 58] have shown FLUENT to be capable of producing reliable results in wide range of problems including airframe noise research, and of resolving the flow structures responsible for noise generation when suitably designed computational mesh and time-step sizes are used. Options for both the explicit as well as the implicit time-stepping are available with the solver. The governing equations are integrated over small finite volumes to yield the equations that conserve the primary variables in each control volume. The governing equations in integral, cartesian form for a control volume V with a differential surface area S are expressed as follows:

$$\frac{\partial}{\partial t} \int_V \mathbf{W} dV + \int_S [\mathbf{F} - \mathbf{G}].dS = \int_V \mathbf{H} dV \qquad (3.11)$$

where the vectors $\mathbf{W}$, $\mathbf{F}$, and $\mathbf{G}$ are given by,

$$\mathbf{W} = \begin{pmatrix} \rho \\ \rho u \\ \rho v \\ \rho w \\ \rho E \end{pmatrix} \quad ; \quad \mathbf{F} = \begin{pmatrix} \rho \mathbf{v} \\ \rho \mathbf{v} u + p\mathbf{i} \\ \rho \mathbf{v} v + p\mathbf{j} \\ \rho \mathbf{v} w + p\mathbf{k} \\ \rho \mathbf{v} E + p\mathbf{v} \end{pmatrix} \quad ; \quad \mathbf{G} = \begin{pmatrix} 0 \\ \tau_{xi} \\ \tau_{yi} \\ \tau_{zi} \\ \tau_{ij} u_j + \mathbf{q} \end{pmatrix}$$

and the vector $\mathbf{H}$ contains the source terms such as body forces and energy sources. The variables τ and $\mathbf{q}$ represent the viscous stress tensor and the heat flux terms, respectively. For this research work, coupled implicit formulation of the solver with a 'QUICK' numerical scheme had been employed. QUICK discretization scheme [59] is based on a weighted average of the second-order-upwind and central

interpolations of variables and it can be used to compute a higher-order value of the convected variable at a cell face for domains with quadrilateral and hexahedral grid cells. QUICK scheme is generally more accurate and is preferred in simulation cases with structured grids and hence has been used here. Coupled implicit solver in FLUENT is recommended for compressible flow simulations and aeroacoustic problems. Also, the implicit solver will generally converge much faster than the explicit solver. Further details of the flow solver set up is presented in Table 4.3 in Chapter 4.
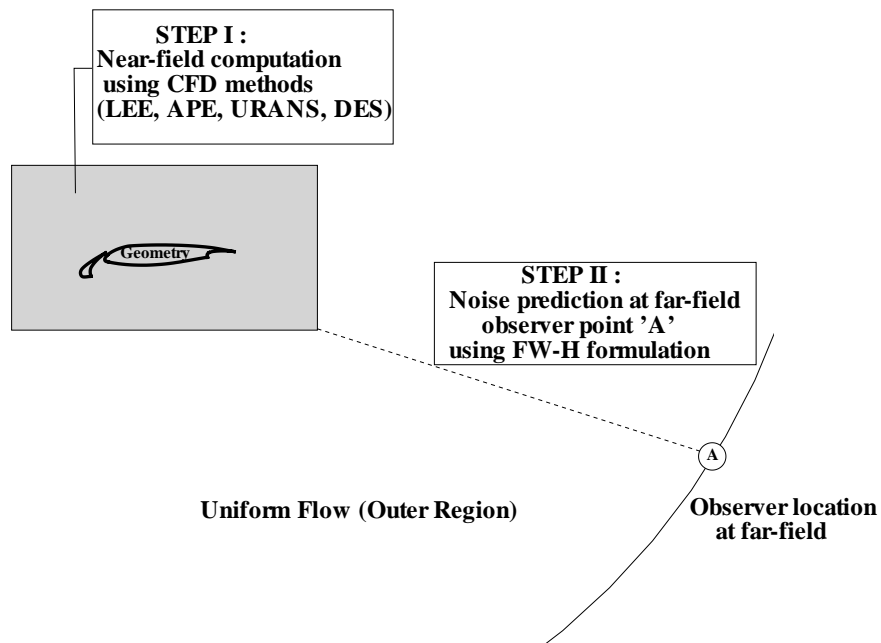
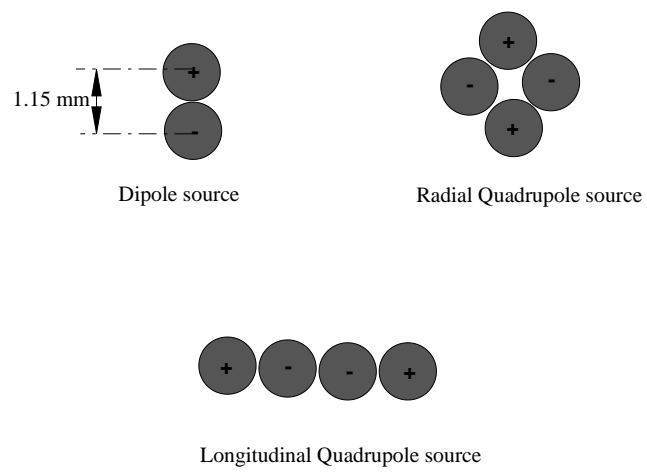FIGURE 3.1: Schematic of the two-step computational procedure.

FIGURE 3.2: A schematic of acoustic sources

Chapter 4

LEE and APE Computations

The numerical results from the LEE and the APE simulations are presented in this chapter. Acoustic analysis was performed to study sound radiation.

4.1   Geometrical Setup and Grid

Numerical simulations were performed in 2D and 3D configurations for the multi-element wing considered in this work. Dipole as well as quadrupole source terms were used to study the acoustic propagation and the effect of source frequency on the sound directivity. Although this project is mainly concerned with the 3D geometry, 2D simulations require less computational power and hence were used to investigate the variations in the sound directivity with frequency and background mean flow. The computational domain for the LEE simulation consisted of a part of a main wing and a slat. Geometrical detail and solver settings used are summarized in Table 4.1.

A total of approximately 32000 grid points were used to construct the 2D grid. Slat wing geometry and the source locations are shown in Figures 4.1 and 4.2. Figure 4.1 also shows the FW-H integration surface used to compute farfield sound pressure level. Table 4.2 lists all the computational cases studied in this project. Case 3 was also solved for three different source locations to study the effect of varying source location on the sound directivity. All the cases except Cases No. 8 and 9 were also simulated with a background mean flow. The grid used for 2D computation is shown in Figure 4.3.

3D grids were designed so that an identical grid topology can be used for both

TABLE 4.1: Geometrical Details

Parameters	Settings
Mean aerodynamic chord (c)	0.728m
Slat angle (in degree)	24.4
Slat gap (as percent of c)	1.99
Slat overhang (as percent of c)	-0.08
Angle of attack (in degree)	0
Flow Mach number	0
Frequency	$500Hz$ to $10kHz$

the wing with and without slat track cases. A total of approximately 900000 grid points were used for the 3D computation at a frequency of 4kHz. For 8kHz and the 10kHz cases, a total of 3000000 grid points were used to construct the computational domain. All the grids (including 2D) were generated to achieve a points per wavelength (PPW) of at least 10. Figure 4.4 shows the 3D grid domain used in the 3D computations.

Table 4.2: List of computed cases

LEE and APE computation cases				
Case No.	Dimension	Frequency	Grid Points (Approx.)	Source Type
1.	2D	500 Hz	32000	Dipole
2.	2D	1 kHz	32000	Dipole
3.	2D	2 kHz	32000	Dipole
4.	2D	4 kHz	32000	Dipole
5.	2D	2 kHz	32000	Quadrupole
6.	2D	4 kHz	32000	Quadrupole
7.	3D	4 kHz	900000	Dipole
8.	3D	8 kHz	3000000	Dipole
9.	3D	10 kHz	3000000	Dipole

4.2   Numerical Results

4.2.1   Two-dimensional study

Initial computations were performed to validate that the LEE and the APE system of equations were equivalent. The computations were performed without mean flow for a longitudinal quadrupole source for the identical geometry using the LEE and the APE solvers. The FW-H solution was obtained for 100 equi-spaced observer locations located around a circle of radius $100m$ with the centre at the slat cove. The directivity in Figure 4.5 shows that two methods are equivalent.

Background mean flow   To study the effects of mean flows in the source propagation, background mean flow is required for the APE solver. Viscous Navier-Stokes simulations were performed in Fluent to extract background mean flow. Steady simulation for 2D grid was performed with the flow conditions similar to typical aircraft landing configurations. Details of the boundary conditions and the flow properties used for the simulations are summarized in Table 4.3.

Table 4.3: 2D flow solver setup parameters

2D steady fluent solver		
Parameters	**Symbol**	**Setup Details**
Mesh Type	-	2D structured Quad
Number of Cells	-	Between 100,000 to 150,000
Turbulence Solver		
Turbulence Model	-	Spalart-Allmaras
Discretization		
Modified Turbulent Viscosity	ν_t	Second Order
flow field	-	Second Order
Buoyancy Forces	F	OFF
Materials		
Density	ρ	Ideal gas
Continued ...		

Table 4.3: (continued)

2D flow solver setup parameters (continued)		
Parameters	**Symbol**	**Setup Details**
Viscosity	μ	Sutherland Law
Boundary Conditions		
Operating Pressure	p_{op}	0.0
Gauge Pressure	p_{gauge}	$101325 Pa$
Freestream Mach Number	M	0.2
Main Element Angle of Attack	α	0^0
Slat Deflection Angle	δ_s	24.4^0 fixed
Slat Overlapp (as % of c^1)	$\o_s$	1.99 fixed
Slat Gap (as % of c)	g_s	0.08 fixed
Freestream Turbulence Intensity	I	1%
Freestream Turbulence Viscosity Ratio	$\frac{\nu_t}{\nu}$	10
Reynolds Number	Re	3.46×10^6
The End		

The grid used to calculate the mean flow is completely different than the one required for APE simulation because the mean flow grid requires fine cells near the wall to resolve the boundary layer and the computational domain is relatively large to ensure that the farfield boundary is far enough from the wing to maintain freestream values of the flow variables at the farfield. In the case of APE simulation, however, the smallest cell size is governed by the PPW requirement to resolve the wave propagation accurately. Also, unlike the large domain required in the viscous case, a relatively small domain which includes all the important surfaces that may affect the wave propagation (in this case full wing is not necessary) and a transparent farfield boundary condition to avoid waves reflecting back to the domain is required for the APE. Hence, the mean flow calculated in relatively fine

---

[1]c is the fully retracted chord length of the wing.

viscous grid was then extracted for the relatively coarse APE grid by interpolation. The interpolation is performed in Tecplot and the interpolating algorithm used is based on inverse-distance method. The inverse-distance algorithm [60] can be described as follow. The value of a variable at a point in the destination zone (APE grid in this case) is calculated as a function of the selected data points in the source zone (viscous grid). The value at each point in the source zone is weighted by a weighting function whose value is dependent on the inverse of the distance between the source data point and the destination data point. The interpolation algorithm and the equation for the weighting function can be expressed as,

$$\varphi^d = \frac{\sum\limits_{i=1}^{n} \beta_i \varphi_i^s}{\sum\limits_{i=1}^{n} \beta_i} \tag{4.1}$$

where φ^d is the variable to be interpolated in the destination zone, φ^s is the variable in the source zone, β_i the value of weighting function at i^{th} location and n the number of points in the source zone used (8 in this case) to interpolate the value at each destination point. The weighting function is evaluated as,

$$\beta_i = d^{-m} \tag{4.2}$$

where d is the distance between the source point and the destination point and m is the exponent specified (3.5 was used in this case) during the interpolation.

Figure 4.6 show the domains for APE and mean flow calculations. Interpolated mean velocity contours in 2D APE grid is shown in Figure 4.7. After interpolation, smoothing was applied to the interpolated mean flow variables to remove peaks, plateaus and noise from the data. The smoothing algorithm in Tecplot is based on a simple Jacobi relaxation technique and is primarily designed for removing local peaks in the solution. Figure 4.8 shows the interpolated mean velocity contours at a section plane through the mid-span of the 3D wing.

The APE simulations were run with a dipole source at the slat trailing edge for four different cases with frequencies varying from 500 Hz to 4kHz. Both the cases with and without a background mean flow were considered. Figure 4.9 shows the contours of acoustic pressure for a 2D wing with and without mean flow. In Figure 4.10 the effects of mean flow on sound directivities for a dipole source are compared.

From Figure 4.10, the effect of the mean flow in the sound directivity is evident. At 500Hz, the lower lobe peak of the directivity is shifted by 22.3 degrees in counter-clockwise direction and the peak SPL is increased by 0.5dB to 21.5dB due to the mean flow. At 1kHz, lower peak occurs at the same angular location (305 degree) for both cases with and without background meanflow, although the directivity shows some effect due to presence of background meanflow i.e a minor lobe appears at an observer angle of 23 degree. At 2kHz frequency, the peak SPL is increased by 1.0dB to 55.2dB and the lower peaks occur at an angle of 330 degree for both the cases. For the 4kHz case, presence of background meanflow causes an increase in the lower SPL peak by 0.75dB. Apart from the lower peak, the presence of a meanflow also changes the other lobes in the directivity as shown in Figure 4.10. Hence, the background meanflow causes Doppler shift on the directivity and it causes change in both the SPL peaks as well as the angle at which these peaks occur. It can also be seen that the directivity pattern for the dipole changes significantly as frequency is increased. This is caused by the source becoming non-compact as the frequency increases. The non-compact dipole source has the effect equivalent to a quadrupole source [61] and this is evident from Figure 4.10. To illustrate this point, additional simulations were run for a quadrupole source at 2kHz and 4kHz. The directivity patterns of Figure 4.11 resembles with those in Figure 4.10 for the frequencies, 2kHz and 4kHz.

When the source is non-compact the farfield sound directivity patterns of the dipole and quadrupole sources are similar. In fact, surface contribution from non-compact dipole is comparable to that of turbulence quadrupoles. Hence quadrupole source in such a case can no longer be treated negligible as treated by Curle [61]. Therefore care must be taken while using Curle's formulation to calculate far-field sound.

Simulations were also run with varying source locations at 2kHz to study the effect of source location variation on sound directivity. Sources were placed at slat trailing edge, at the middle of the gap between slat and main element; and a third source was put at a distance equal to 5% of slat gap from the main element. These simulations were run without background mean flow. Figure 4.12 shows the directivity plot for the three cases. From the figure it can be see that change of source location affects the directivity. This can be because the angular location of source relative to slat and the main element is changed with change of source location. This results in the waves being reflected at changed direction, hence the difference in the sound directivity. Figure 4.13 illustrates the effect on waves propagation due to change in source locations. The location of the source, therefore, with respect

to the slat/wing geometry affects the directivity pattern.

4.2.2   Three-dimensional study

The 3D APE simulations were run with a line of dipole source at the slat trailing edge. Two different geometries were considered. The first included a 3D wing with a leading edge slat. The second case was a 3D wing with a leading edge slat and a slat track. The second case was also solved with CFD mean flows. The directivities were obtained for all cases in a plane passing through the mid-section of the slat track. The simulations were run with a dipole source at the slat trailing edge at 4kHz frequency. Figure 4.14 shows the acoustic pressure contours for the two cases. Figure 4.15 compares the directivities for the two cases in absence of a background meanflow.

The acoustic waves in the contour plots of Figure 4.14 for the two cases are similar, i.e. it shows that for the 4kHz source frequency the presence of the slat track has negligible effects on the wave propagation. The directivity plot in Figure 4.15 also confirms that for 4kHz source frequency there is a negligible difference in the acoustic propagation due to the presence of the slat track. The dipole source orientation of 3D wing without slat track and the 2D case is different. Hence, there is a difference in the two directivities pattern. Figure 4.16 represents the directivity comparison for the 3D wing with slat track in presence of a mean flow. The directivity indicates that meanflow results in an increased SPL peak by 0.5 dB and is also shifted by 6 degree in counter-clockwise direction. This is consistent with the observations from the 2D results. t At 4kHz, the acoustic wave length (λ) is 8.5cm and the slat thickness (b) for the model is $3.2cm$ (i.e. $\lambda >$b). Also when λ is greater than b, the reflection and diffraction processes are inefficient [62]. This may be the reason for the negligible effect of the slat track at the low frequency. A frequency which corresponds to a wavelength less than the slat track thickness is considered to be a high frequency and a value which corresponds to a wavelength greater than the slat track thickness is considered a low frequency in this project work. When frequency is increased so that the acoustic wave length becomes close to the slat track thickness, then the reflection and diffraction processes are expected to appear. A wave length of 3.2cm corresponds to a frequency of 10.6kHz. A frequency of 10kHz still falls in low frequency category.

Simulations were also run for 3D wing with a slat track and a 3D wing without a slat track in absence of a background mean flow at 8kHz and 10kHz source

frequency. The nearfield contours are plotted for the 8kHz case in Figures 4.17 and 4.18. The contours clearly show the scattering of the acoustic waves in the presence of the slat track. The diffraction pattern can also be seen near the slat cusp. These phenomena become significant when the acoustic wave length (λ) is smaller that the slat track thickness. Figure 4.21 compares the directivity for the 3D wing with and without a slat track at 8kHz. At an observer at 204 degree counter clockwise position, an enhanced a minor lobe is seen due to the presence of slat track resulting in an increase in SPL by 2 dB. Similarly, minor lobes with noticeably increased SPL peaks also occur at 220 (2 dB increase) and 270 (1 dB increase) degree observer positions. These patterns can be seen more pronounced for 10kHz case in Figures 4.19 and 4.20. As the wave length becomes comparable to the thickness of the slat track, effects of acoustic scattering start to appear. These effects will be more dominant at higher frequencies. Figures 4.22 compares the directivity for the 3D wing with and without a slat track at 10kHz frequency. The effects of the presence of slat track can be seen in the directivity. At an observer at 260 degree position, the slat track causes the increase in SPL by 2.5 dB. Noticeable enhancement of minor lobes also occur at 208 (2.5 dB increase), 215 (2 dB increase) and 245 (0.5 dB increase) degree observer positions. Unlike in 8kHz frequency case, two minor lobes with increased SPL also appear at at 30 (0.5 dB increase), 54 (1.5 dB increase) degree observer positions. Overall SPL peak occurs at 305 degree observer position and the SPL peak for the slat track case is found to increase by 0.25 dB with compared to the wing without the slat track.
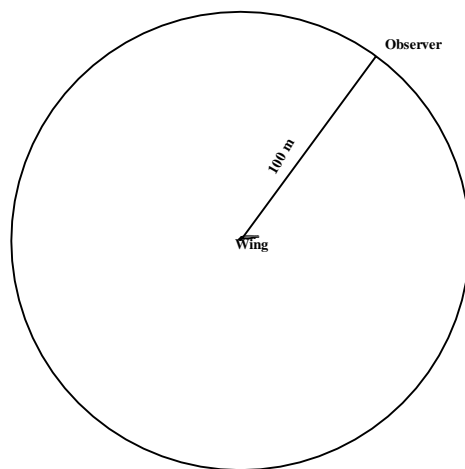
Far-field observers.   Source location and the integration surface.
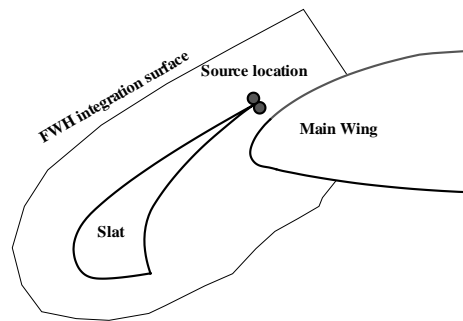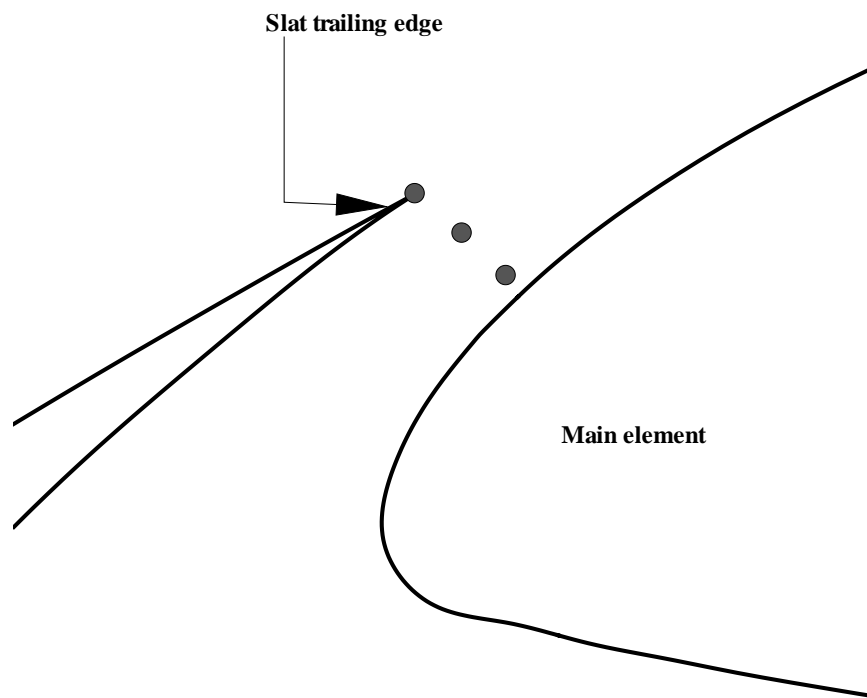
FIGURE 4.1: Geometrical setup.

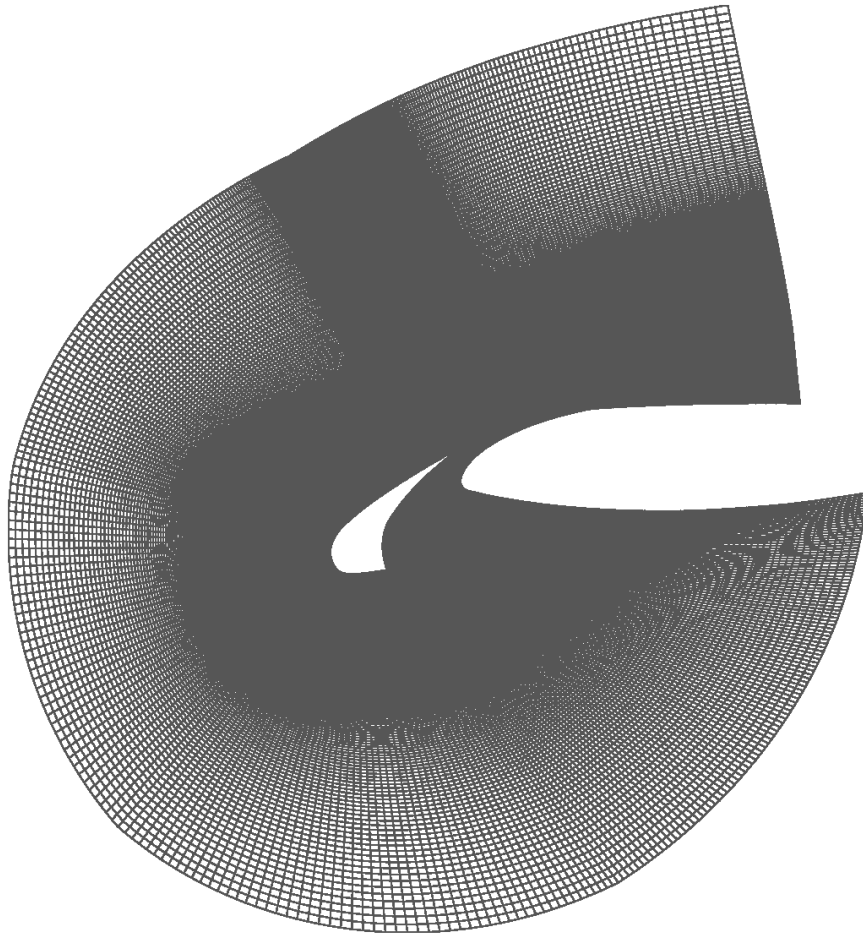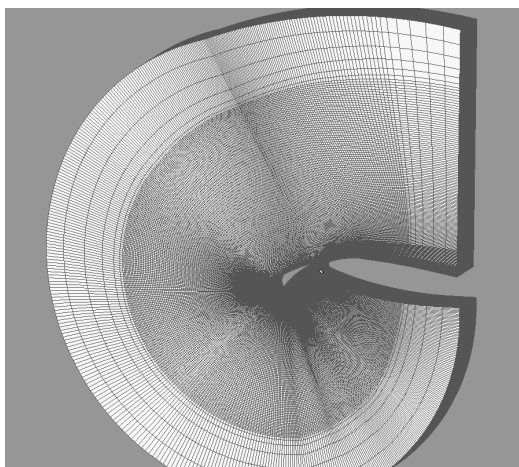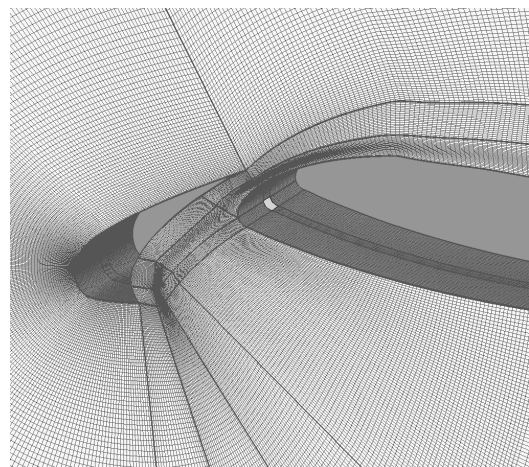FIGURE 4.2: Three different source locations used for the directivity study.

FIGURE 4.3: 2D grid used in the LEE and the APE simulations.

(a) 3D domain.

(b) 3D domain close up view.
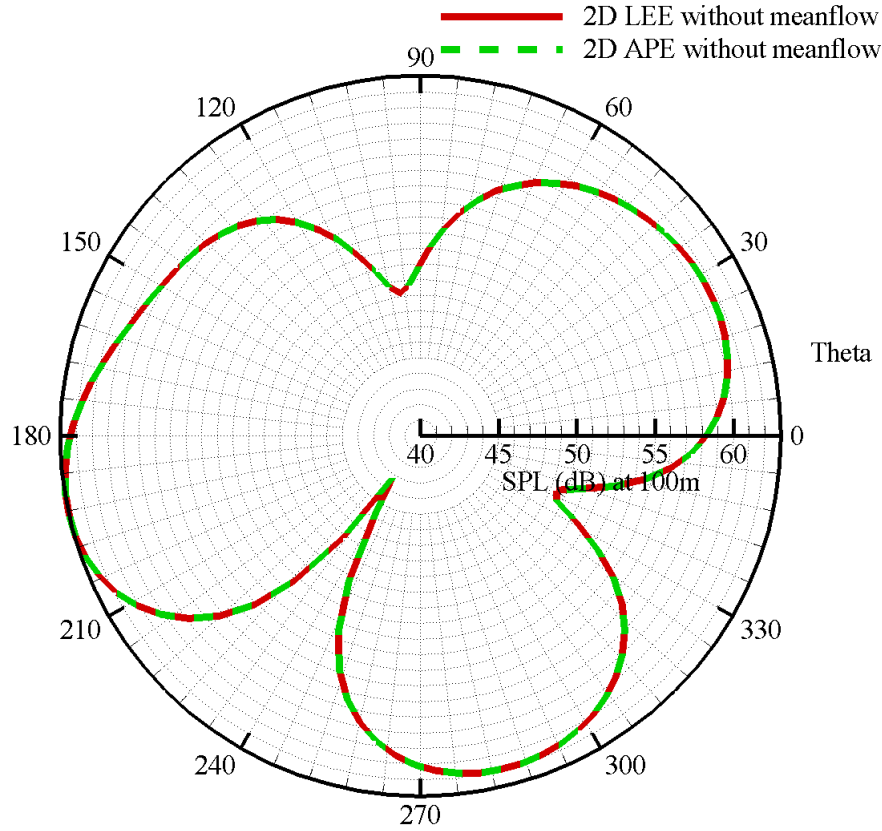
FIGURE 4.4: 3D grid used in APE calculation.

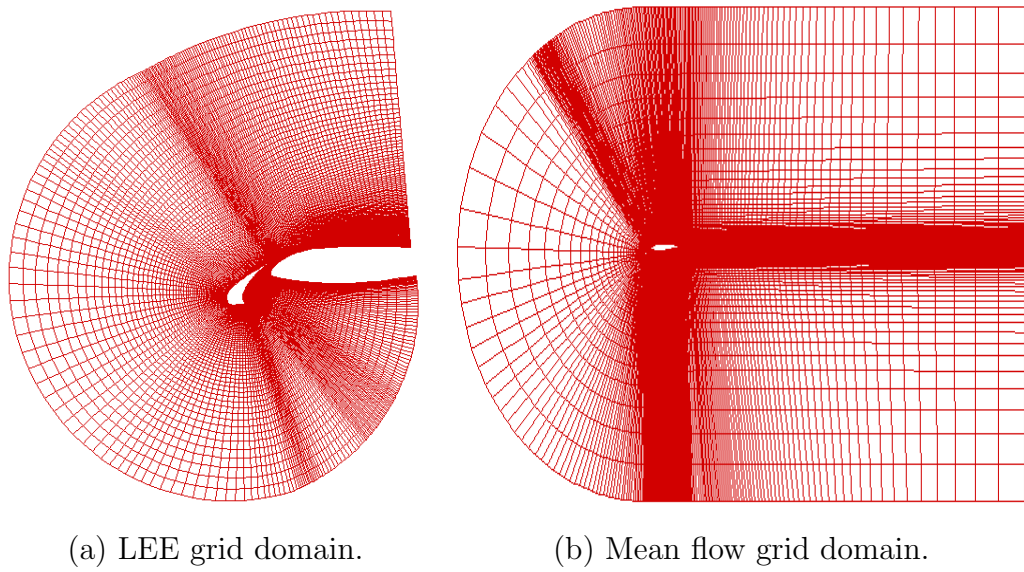FIGURE 4.5: APE and LEE directivity for a quadrupole source, f = 1kHz.

(a) LEE grid domain.

(b) Mean flow grid domain.

FIGURE 4.6: Domains used for the LEE simulation and mean flow computation.
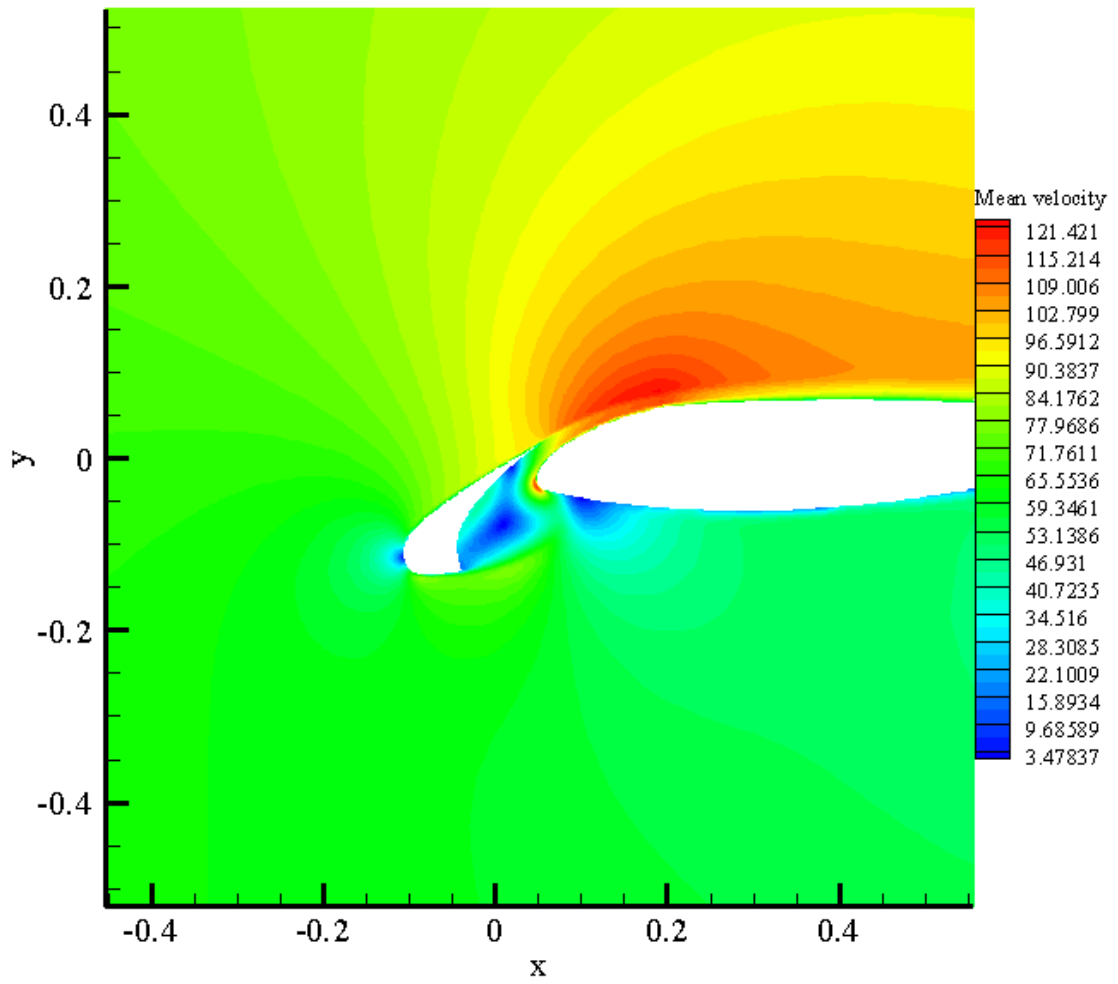
FIGURE 4.7: Interpolated mean velocity contours in 2D APE grid.
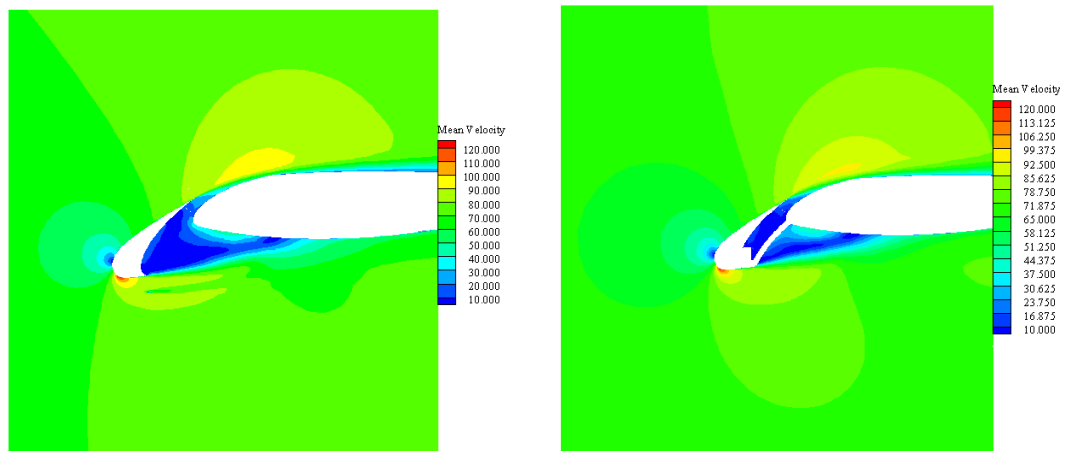
(a) Mid-span of wing-slat model.

(b) Section through middle of slat track.

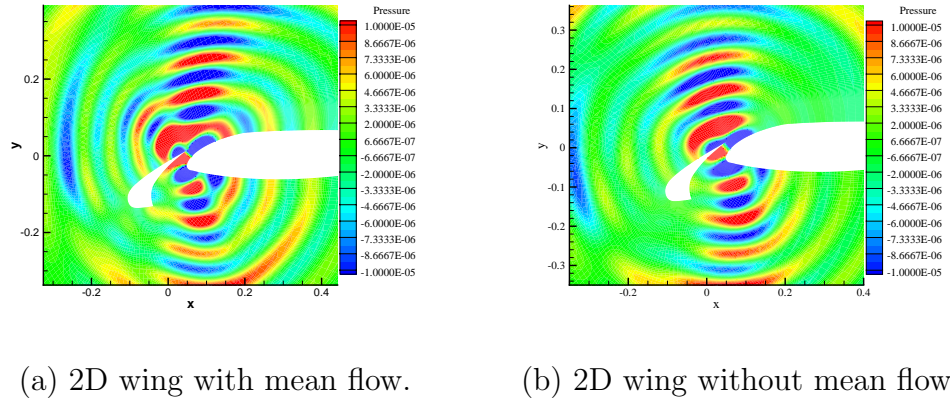FIGURE 4.8: Interpolated mean velocity contours for 3D APE simulations.

(a) 2D wing with mean flow.

(b) 2D wing without mean flow.

FIGURE 4.9: Pressure contours of a dipole source at 4kHz source frequency.

(a) f=500 Hz.

(b) f=1 kHz.

(c) f=2 kHz.

(d) f=4 kHz.
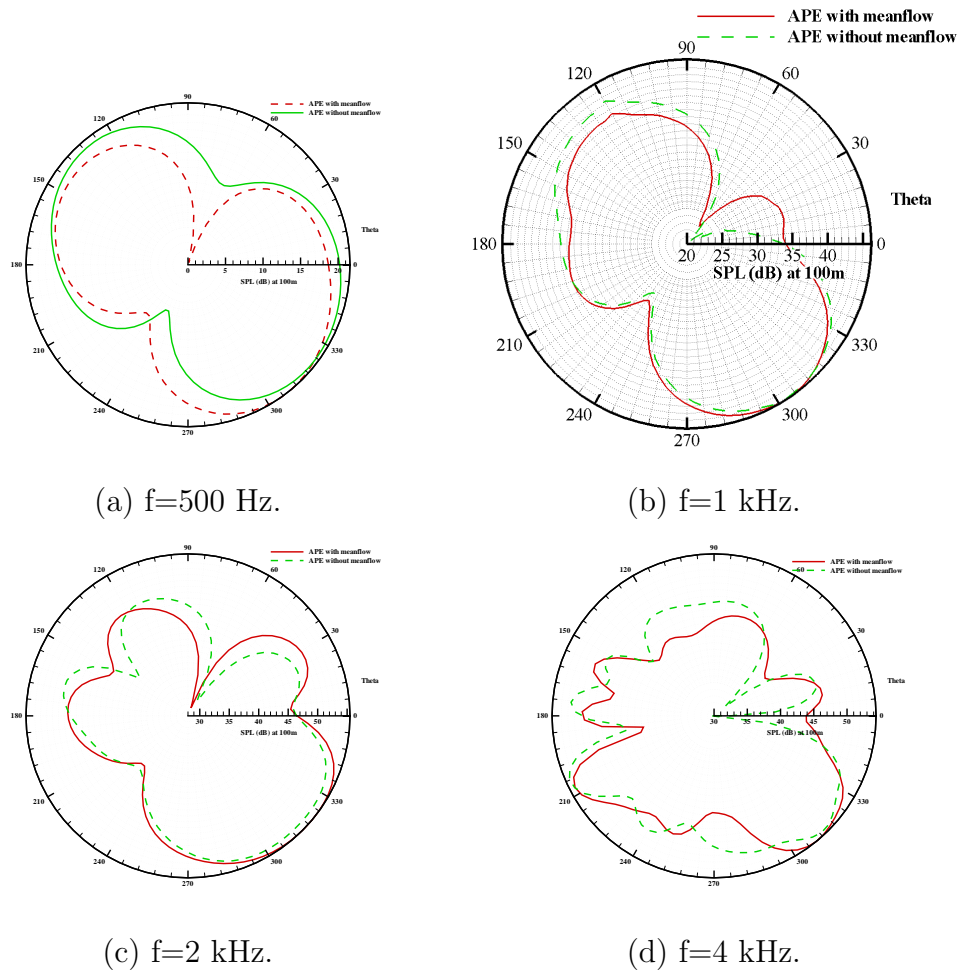
FIGURE 4.10: Effect of mean flow on directivities for dipole source.
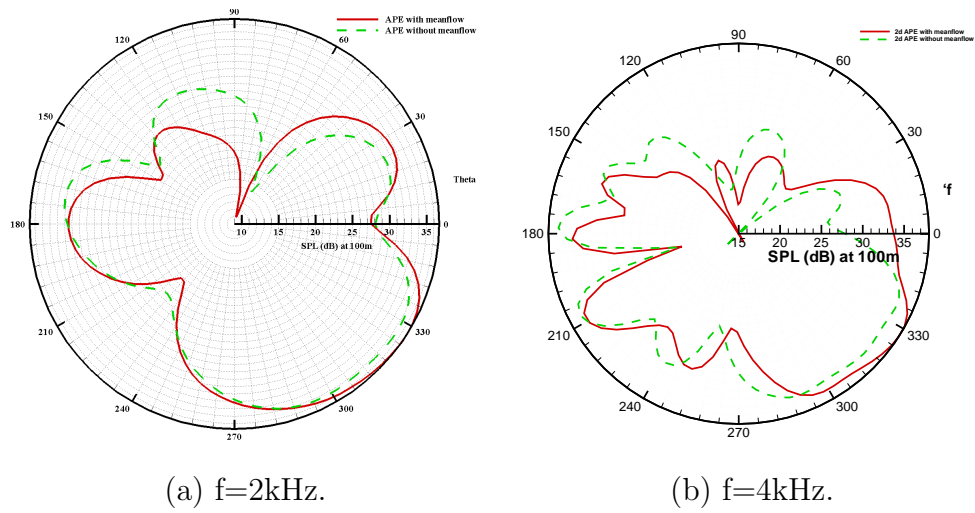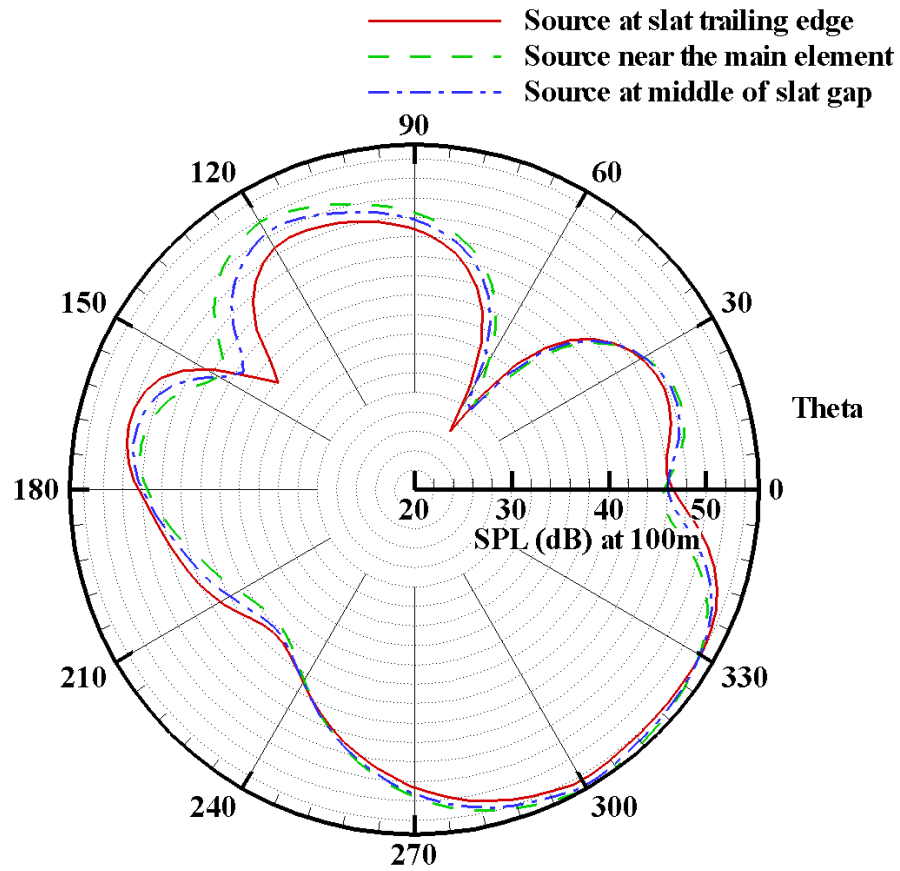
(a) f=2kHz.   (b) f=4kHz.

FIGURE 4.11: Effect of mean flow on directivities for quadrupole source.

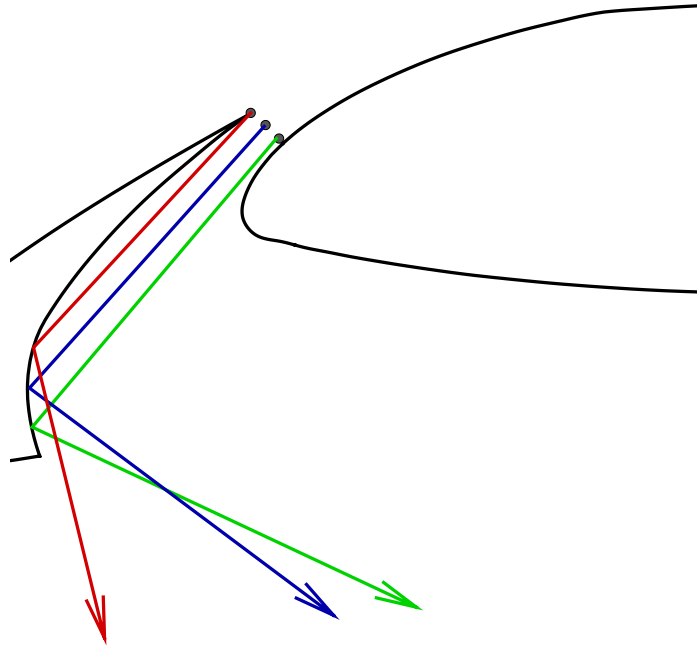FIGURE 4.12: Directivity showing the effect of varying source location, f = 2kHz.
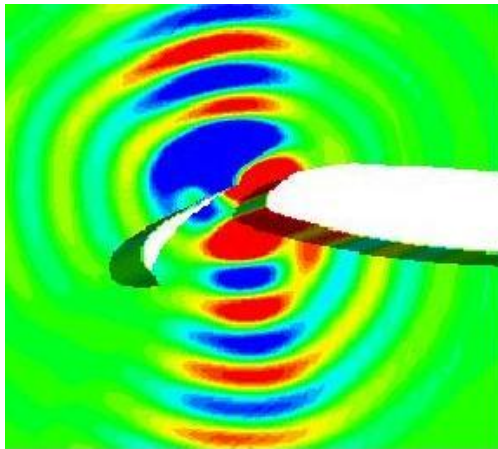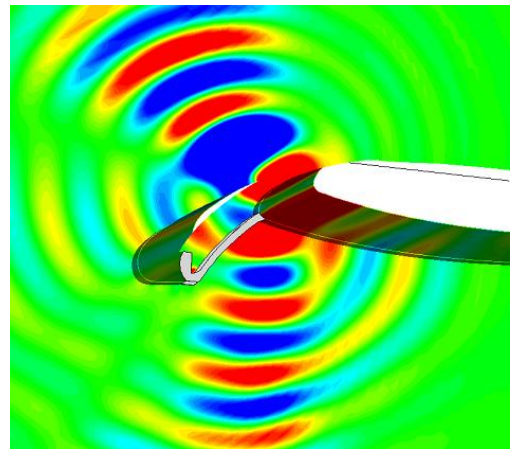
FIGURE 4.13: Waves reflection due to variation in source location.

(a) 3D wing without a slat track.

(b) 3D wing with a slat track.

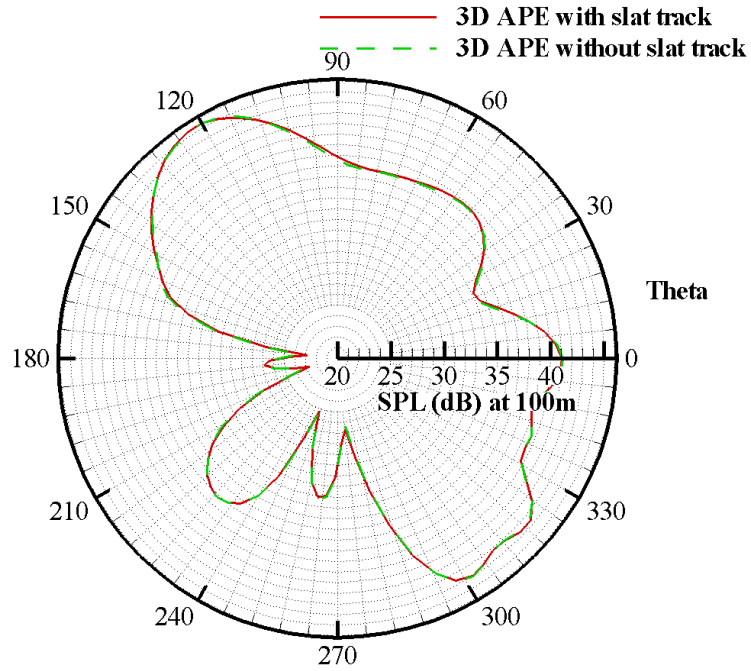FIGURE 4.14: Pressure contours of a dipole source at 4kHz source frequency in absence of background mean flow.

FIGURE 4.15: 3D directivity comparison for a dipole source, f = 4kHz.
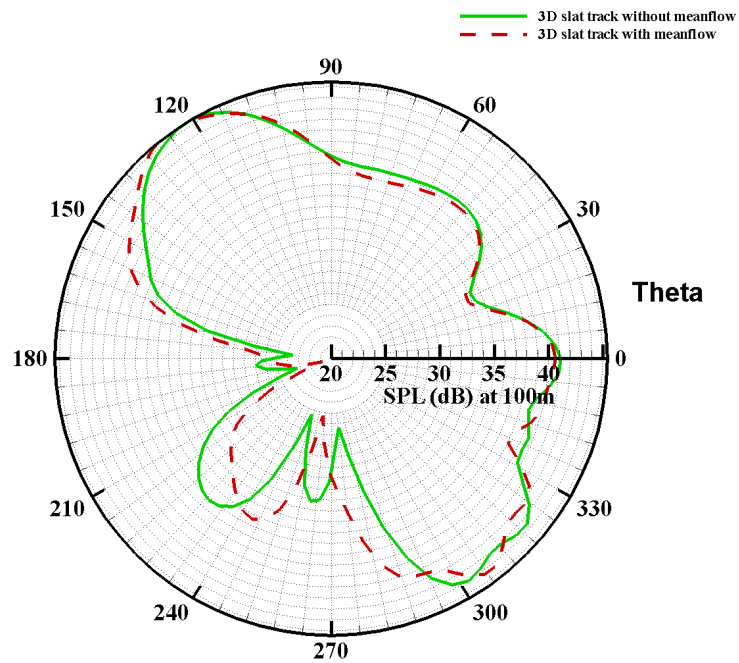
FIGURE 4.16: Effect of mean flow on the directivity of a 3D wing with slat track, f = 4kHz.
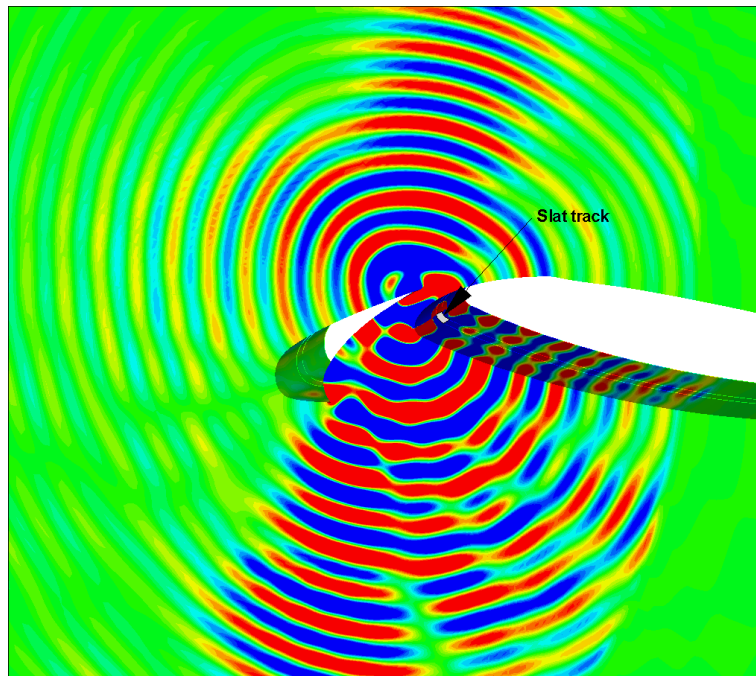
FIGURE 4.17: Pressure contours for a 3D wing with a slat track, f = 8kHz.
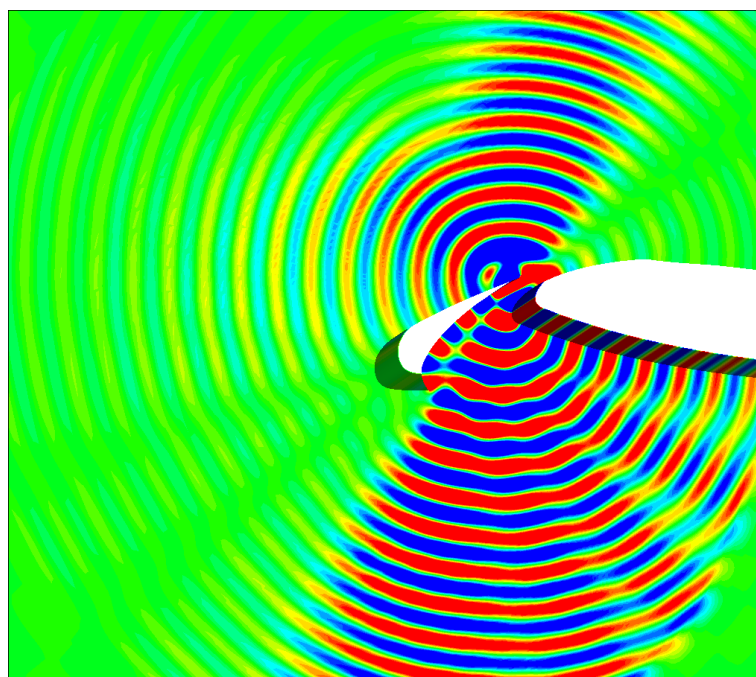
FIGURE 4.18: Pressure contours for a 3D wing without a slat track, f = 8kHz.
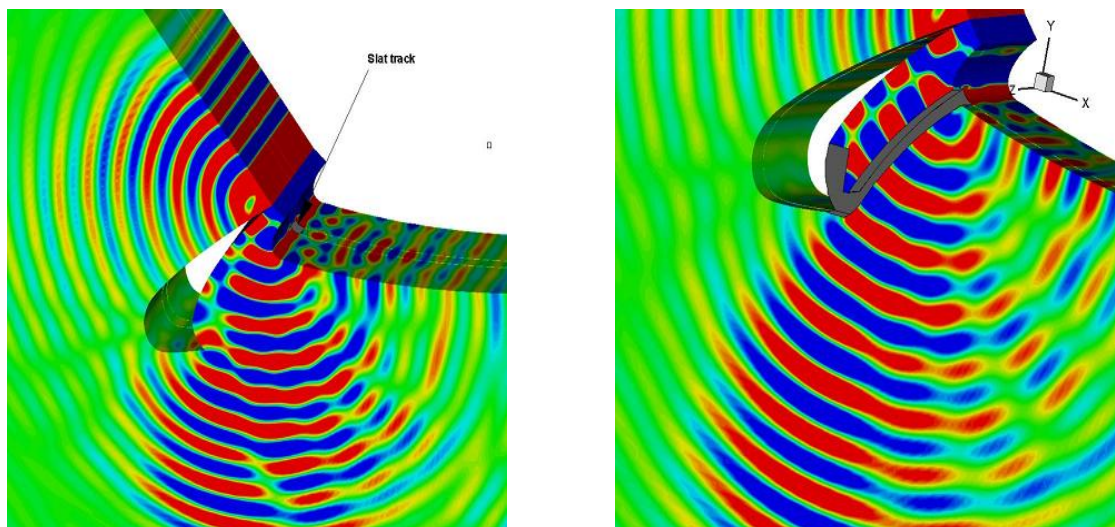
(a) 3D wing with a slat track.   (b) 3D wing with a slat track mid-section view.

FIGURE 4.19: Pressure contours of a dipole source at 10kHz source frequency
in absence of background mean flow.
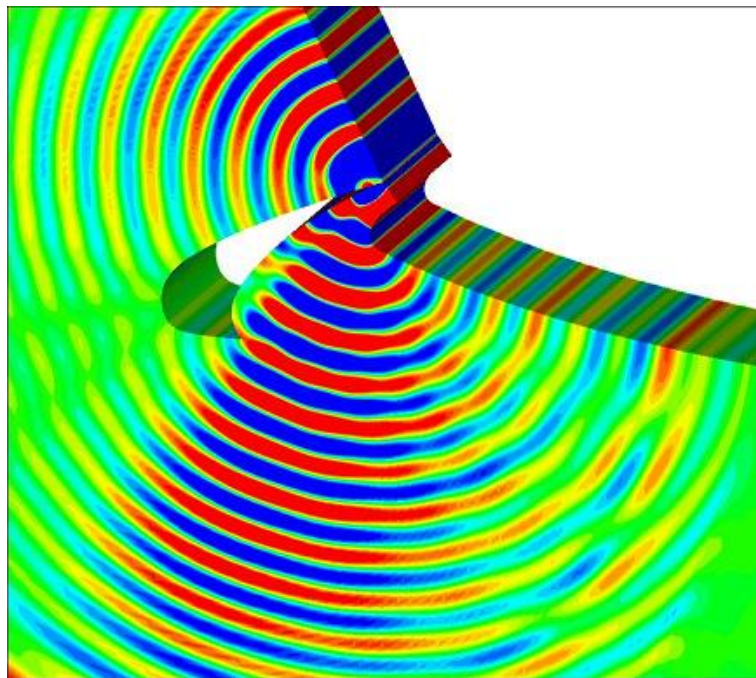
FIGURE 4.20: Pressure contours for a 3D wing without a slat track, f = 10kHz.
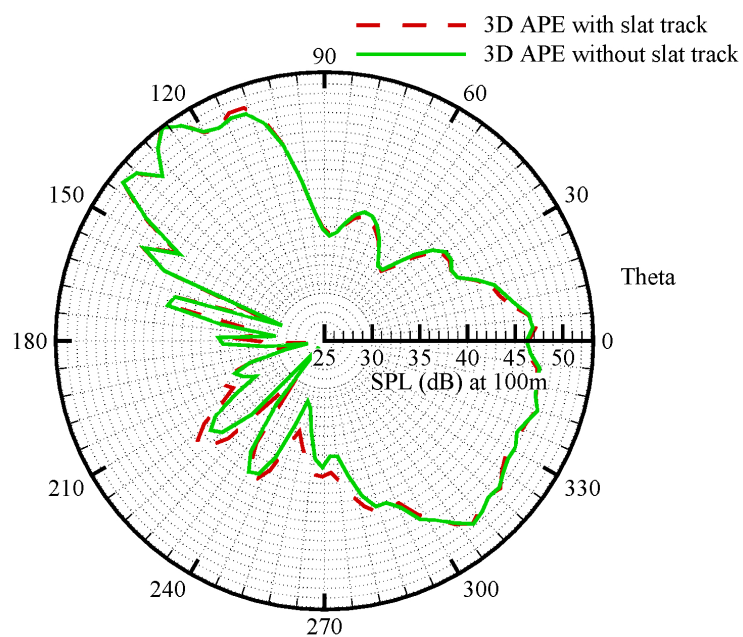
FIGURE 4.21: Directivity comparison for a dipole source, f = 8kHz.

FIGURE 4.22: Directivity comparison for a dipole source, f = 10kHz.

Chapter 5

Conclusions and Future Work

A summary of the main conclusions and the suggested future works are now presented.

5.1 Concluding Remarks

5.1.1 2D APE Results

The numerical results has been obtained for 2D as well as 3D geometries. At 500Hz, the lower peak of the directivity is shifted by 22.3 degrees and the peak SPL is increased by 0.5dB due to the presence of meanflow. At 1kHz, a minor lobe appeared at an observer angle of 23 degree due to presence of background mean flo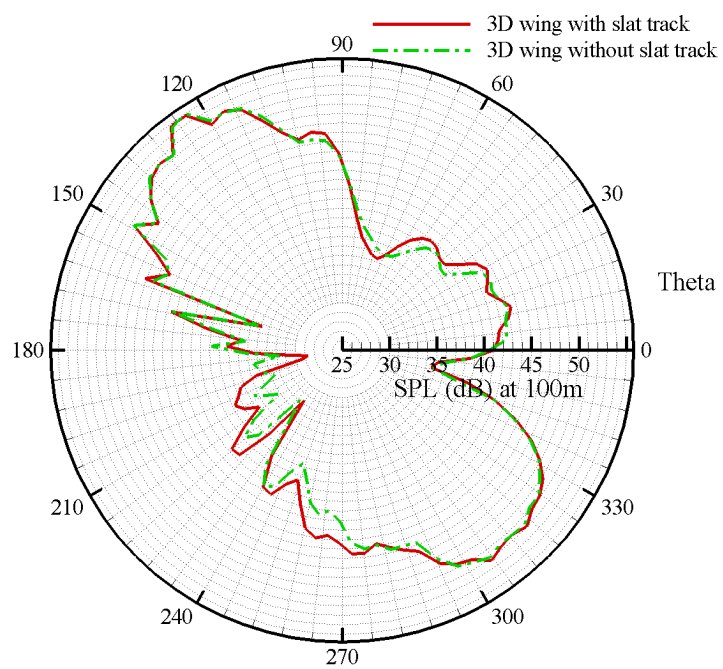w. At 2kHz frequency, the peak SPL is found to increase by 1.0dB and the lower peaks occur at an angle of 330 degree for both the cases. For the 4kHz case, presence of background meanflow causes an increase in the lower SPL peak by 0.75dB. Generally, the background meanflow is found to cause the change in both the SPL peaks as well as the angle at which these peaks occur. It was also found that the directivity pattern for the dipole changes significantly as the frequency was increased. This was the result of the source becoming non-compact as the frequency increased. The study found that the effect of non-compact dipole source resembled that of a quadrupole source. The mean flow had effect of resulting in increased peak and also caused the directivity shift relative to no mean flow case. The 3D simulation with the mean flow also had similar effect as in the 2D results. The shift in the peak of the sound pressure level was also observed in 3D. Hence, mean flow effects both the magnitude of the SPL peak as well as the angle at

which these peaks occur. Sources were placed at slat trailing edge, at the middle of the gap between slat and main element; and a third source was put at a distance equal to 5% of slat gap from the main element to study the effect of source location variation on sound directivity. From the computed result, change of source location was found to affect the directivity. This had an effect of equivalent Doppler shift of the waves as it reflected from the slat. Hence, 2D simulation shows that the main effect of mean flow was to change the SPL peak and to cause a shift in sound directivity.

5.1.2 3D APE Results

The 3D APE simulations studied two different wing geometries. The first included a 3D wing with a leading edge slat and second case was a 3D wing with a leading edge slat and a slat track. The directivity plot at 4kHz source frequency showed a negligible difference in the acoustic propagation due to the presence of the slat track. At this frequency, the wave length is greater than the thickness of the slat track. Hence, there is no significant effect on the diffraction and reflection phenomena.

For the case of 8kHz frequency, enhanced minor lobes were seen in the directivity due to the presence of slat track resulting in an increase in SPL by 2 dB. These patterns were found to be more pronounced for 10kHz case. In this case, the presence of slat track resulted in an increase in SPL by 2.5 dB. Unlike in 8kHz frequency case, two minor lobes with increased SPL also appeared at 30 (0.5 dB increase) and 54 (1.5 dB increase) degree observer positions. Hence 3D result showed that increasing the frequency of the acoustic sources resulted in increased effect of the slat track on the directivity.

5.2 Suggested Future Work

An area of immediate interest is the unsteady viscous simulation of the wing with and without a slat track. This will help to gain a clearer insight into the complex flow region present in the slat cove for the wing slat geometry and complex flowfield around the slat track for the wing with slat track. The source of noise responsible for the excess noise from the slat track can, then, be identified. The far-field radiation of the acoustic source, thus, identified can then be computed using the far-field prediction method based on the solution of FW-H equation.

Bibliography

[1] G. Raman and D. K. McLaughlin. Recent aeroacoustics research in the United States. *Noise and Vibration Worldwide*, 31(10):15–20, 2000.

[2] J. E. Ffowcs Williams and D. L. Hawkings. Sound generation by turbulence and surfaces in arbitrary motion. *Philosophical Transactions of Royal Socciety*, A(264):321–342, 1969.

[3] Michael Pott-Pollenske, Werner Dobrzynski, Heino Buchholz, Sebastien Guerin, Gerd Saueressig, and Ullrich Finke. Airframe noise characteristics from flyover measurements and predictions. *AIAA-paper-2006-2567*, May 8-10 2006. 12th AIAA/CEAS Aeroacoustics Conference,Breckenridge, Cambridge, Massachusetts.

[4] M.G. Smith, B. Fenech, Leung Choi Chow, N. Molin, W. Dobrzynski, and Chistelle Seror. Control of noise sources on aircraft landing gear bogies. *AIAA-paper-2006-2626*, May 8-10 2006. 12th AIAA/CEAS Aeroacoustics Conference,Breckenridge, Cambridge, Massachusetts.

[5] Christodoulos Andreou, Will Graham, and Ho-Chul Shin. Aeroacoustic study of airfoil leading edge high-lift devices. *AIAA-paper-2006-2515*, May 8-10 2006. 12th AIAA/CEAS Aeroacoustics Conference,Breckenridge, Cambridge, Massachusetts.

[6] Geoffrey M. Lilley. A quest for quiet commercial passenger transport aircraft for take-off and landing. *AIAA-paper-2004-2922*, May 10-12, 2004. 10th AIAA/CEAS Aeroacoustics Conference , Manchester, United Kingdom.

[7] R. Davy and H. Remy. Airframe noise charateristics on a 1/11 scale airbus model. *AIAA-paper-98-2335*, June 2001.

[8] M. J. Lighthill. On sound generated aerodynamically. i. general theory. *Proceedings of Royal Society*, A(211):564–587, 1952.

[9] F. farassat. Introduction to generalized functions with applications in aerodynamics and aeroacoustics. *NASA Technical Paper-3428*, May 1994. National Aeronautics and Space Administration, Langley Research Center, Hampton, Virginia 23681-2199.

[10] Valana L. Wells Renaut and Rosemary A. Computing aerodynamically generated noise. *Annual Review of Fluid Mechanics*, 29:161–199, 1997.

[11] N. Curle. The influence of solid boundaries upon aerodynamic sound. *Proceedings of Royal Society*, A(231):505–514, 1955.

[12] F. Farasaat and G. P. Succi. The prediction of helicopter discrete frequency noise. *Vertica*, 7:309–320, 1983.

[13] P. Di Francescantonio. A new boundary integral formulation for the prediciton of sound radiation. *Journal of Sound and Vibration*, 202(4):491–509, 1997.

[14] Bart A. Singer and Yueping Guo. Development of computational aeroacoustic tools for airframe noise calculations. *International Journal of Computational Fluid Dynamics*, 18(6):455–469, August 2004.

[15] Konstantin A. Kurbatskii and Reda R. Mankbadi. Review of computational aeroacoustics algorithms. *International Journal of Computational Fluid Dynamics*, 18(6):533–546, August 2004.

[16] Christopher K. W. Tam and Jay C. Webb. Dispersion-relation-perserving finite difference schemes for computational acoustics. *Journal of Computational Physics*, 107:262–281, 1993.

[17] Jae Wook Kim and Duck Joo Lee. Optimised compact finite difference schemes with maximum resolution. *AIAA Journal*, 34(5):887–893, May 1996.

[18] R. Hixon. Prefactored small-stencil compact schemes. *Journal of Computational Physics*, 165:522–541, 2000.

[19] Graham Ashcroft and Xin Zhang. Optimized prefactored compact schemes. *Journal of computational physics*, 190:459–477, 2003.

[20] James R. DeBonis and James N. Scott. Study of the error and efficiency of numerical schemes for computational aeroacoustics. *AIAA Journal*, 40(2):227–234, 2002.

[21] Man Mohan Rai. A conservative treatment of zonal boundaries for euler equation calculations. *Journal of Computational Physics*, 62:472–503, 1986.

[22] Man Mohan Rai. An implicit, conservative, zonal-boundary scheme for euler equation calculations. *Computers and Fluids*, 14:295–319, 1986.

[23] A. Lerat and Charles Z. N. Wu. Stable conservative multidomain treatments for implicit Euler solvers. *Journal of computational physics*, 123:45–64, 1996.

[24] A. Benkenida, J. Bohbot, and J. C. Jouhaud. Patched grid and adaptive mesh refinement strategies for the calculation of the transport vortices. *International Journal of Numerical Methods in Fluids*, 40:855–873, 2002.

[25] Christopher K. W. Tam. Computational aeroacoustics examples showing the failure of the acoustic analogy theory to identify the correct sources. *Journal of Computational Acoustics*, 10(4):387405, 2002.

[26] S. Kim, Y. Dai, E. K. Koutsavdis, S. Sovani, N. A. Kadam, and K. M. R. Ravuri. A versatile implementation of acoustic analogy based noise prediction method in a general-purpose cfd code. Number AIAA–2003–3202, Hilton Head,South Carolina, USA, May 2003. 9th AIAA/CEAS Aeroacoustics Conference and Exhibit.

[27] K. S. Brentner. Prediction of helicopter discrete frequency rotor noise - a computer program incorporating realistic blade motions and advanced formulations. *NASA/TM-1986-87721*, October 1986.

[28] Susan Olson, Flint O. Thomas, and Robert C. Nelson. A preliminary investigation into slat noise production mechanism in a high-lift configurations. *AIAA-paper-2000-4508*, 2000.

[29] Bart A. Singer, David P. Lockard, Kenneth S. Brentner, Mehdi R. Khorrami, Mert E. Berkman, and Meelan Choudhari. Computational aeroacoustic analysis of slat trailing edge flow. *AIAA-paper-1999-1802*, 1999.

[30] Eric Manoha, Catherine Herrero, Pierre Sagaut, and Stephane Redonnet. Numerical prediction of airfoil aerodynamic noise. *AIAA-paper-2002-2573*, June 17-19, 2002. 8th AIAA/CEAS Aeroacoustics Conference,Breckenridge, Colorado, USA.

[31] Kenneth S. Brentner and F. Farassat. Analytical comparison of the acoustic analogy and kirchhoff formulation for moving surfaces. *AIAA Journal*, 36(8):1379–1386, 1998.

[32] Jay H. Kasper, David P. Lockard, Mehdi R. Khorrami, and Craig L. Streett. Investigation of volumetric sources in airframe noise simulations. *AIAA-paper-2004-2805*, May 10-12 2004. 10th AIAA/CEAS Aeroacoustics Conference , Manchester, United Kingdom.

[33] D. G. Crighton, A. P. Dowling, Ffowcs J. E. Williams, M. Heckl, and F. G. Leppington. Noise source mechanisms. *Acoustics Lecture Note series*, pages 334–342, 1992.

[34] Jeff M. Mendoza, Thomas F. Brooks, and William M. Humphreys. Aeroacoustic measurements of a wing/slat model. *AIAA-paper-2002-2604*, June 17-19 2002. 8th AIAA/CEAS Aeroacoustics Conference,Breckenridge, Colorado, USA.

[35] F. O. Thomas, R. C. Nelson, and X. Liu. Experimental investigation of the confluent boundary layer of a high-lift system. *AIAA Journal*, 38(6):978–988, 2000.

[36] Mehdi R. Khorrami, Meelan M. Choudhari, and Mert E. Berkman. Unsteady flow computations of a slat with a blunt trailing edge. *AIAA Journal*, 38(11):2050–2058, 2000.

[37] Bruce L. storms, Julie A. Hayes, Patrick J. Moriarty, and James C. Cross. Aeroacoustic measurements of slat noise on a three-dimensional high-lift system. *AIAA-paper-1999-1957*, 1999.

[38] Mehdi Khorrami and David P. Lockard. Effects of geometric details on slat noise generation and propagation. *AIAA-paper-2006-2664*, May 8-10 2006. 12th AIAA/CEAS Aeroacoustics Conference, Cambridge, Massachusetts.

[39] B. L. Storms, J. C. Ross, W. C. Horne, J. A. Hayes, R. P. Dougherty, J. R. Underbrink, D. F. Scharpf, and P. J. Moriarty. An aeroacoustic study of an unswept wing with three-dimensional high-lift system. *NASA TM-1998-112222*, 1998.

[40] M. G. Macaraeg. Fundamental investigations of airframe noise. *AIAA-paper-1998-2224*, 1998.

[41] M. A. Takallu and K. R. Laflin. Reynolds-averaged navier-stokes computations of two partial-span flap wing experiments. *AIAA-paper-1998-0701*, 1998.

[42] Mehdi Khorrami, Meelan Choudhari, Bart A. Singer, David P. Lockard, and Craig L. Streett. In search of physics: The interplay of experiment and computation in slat aeroacoustics. *AIAA-paper-2003-0980*, January 6-9 2003. 41st Aerospace Sciences Meeting and Exhibit, Reno, Nevada.

[43] Christopher K. W. Tam and Nikolai Pastouchenko. Gap tones. *AIAA Journal*, 39(8):1442–1448, 2001.

[44] Anurag Agarwal and Philip J. Morris. Investigation of the physical mechanism of tonal sound generated by slats. *AIAA-paper-2002-2575*, June 17-19 2002. 8th AIAA/CEAS Aeroacoustics Conference, Breckenridge, Colorado, USA.

[45] K. Takeda, X. Zhang, and P. A. Nelson. Computational aeroacoustic simulations of leading-edge slat flow. *Journal of Sound and Vibration*, 270:559–572, 2004.

[46] Mehdi Khorrami, Bart A. Singer, and Mert E. Berkman. Time-accurate simulations and acoustic analysis of slat free-shear layer. *AIAA-paper-2001-2155*, 28-30 May, 2001. 7th AIAA/CEAS Aeroacoustics Conference, Maastricht, Netherlands.

[47] Mehdi Khorrami, Bart A. Singer, and D. Lockard. Time-accurate simulations and acoustic analysis of slat free-shear layer: part ii. *AIAA-paper-2002-2579*, June 17-19, 2002. 8th AIAA/CEAS Aeroacoustics Conference, Breckenridge, Colorado, USA.

[48] Werner Dobrzynski, Kiyoshi Nagakura, Burkhard Gehlhar, and Andreas Buschbaum. Airframe noise studies on wings with deployed high-lift devices. *AIAA-paper-1998-2337*, June 2-4 1998. 8th AIAA/CEAS Aeroacoustics Conference, Toulouse, France.

[49] M Terracol, E. Labourasse, E. Manoha, and P. Sagaut. Simulation of 3d unsteady flow in a slat cove for noise prediction. *AIAA-paper-2003-3110*, May 12-14 2003. 9th AIAA/CEAS Aeroacoustics Conference and Exhibit,Hilton Head,South Carolina, USA.

[50] Meelan M. Choudhari, M. R. Khorrami, M. E. Berkman, and S.S. Sadowski. Investigation of high-lift flowfield of an energy effiicient transport wing. *Journal of Aircraft*, 37(1):45–52, 2000.

[51] Philippe Petitjeans. Stretching of a vortical structure: filaments of vorticity. *Euro Physics News*, 34(1), 2003.

[52] J Reichenberger. Design of combined streamlined slat track and track opening fairings. *Unpublished paper*, July 2002. EADS-Deutschland GmbH Corporate Research Center Germany.

[53] R. Ewert and W. Schröder. Acoustic perturbation equations based on flow decomposition via source filtering. *Journal of Computational Physics*, 188:365–398, 2003.

[54] R. Ewert. Slat noise trend predictions using caa with stochastic sound sources from a random particle mesh method. *AIAA-paper-2006-2667*, May 8-10 2006.

[55] S. K. Richards. *Acoustic Wave Propagation Using Computational Aeroacoustic Methods*. PhD thesis, University of Southampton, Nov 2004.

[56] zhaokai Ma. *Slat Noise Attenuation with Acoustic Liner Treatment*. PhD thesis, University of Southampton, Nov 2004.

[57] F. Q. Hu, M. Y. Hussaini, and J. Manthey. Low-dissipation and -dispersion runge-kutta schemes for computational acoustics. *Journal of Computational Physics*, 124:177–191, 1996.

[58] F. Mathey, O. Morin, B. Caruelle, and K. Debatin. Simulation of aeroacoustic sources in aircraft climate control systems. Number AIAA–2006–2493, Cambridge, Massachusetts, USA, May 2006. 12th AIAA/CEAS Aeroacoustics Conference and Exhibit.

[59] Fluent Inc. *FLUENT 6.2 User Guide*, 2005.

[60] Tecplot Inc. *Tecplot 360 user manual*, 2006.

[61] M. S. Howe. Radiations from a non-compact source. *Acoustics Lecture Note series*, pages 37–39, 1992.

[62] J. Astley. Lecture notes on mathematical methods of acoustics. *Acoustics Lecture Notes 2004, University of Southampton*, 2004.

.1   Derivation of Source Filtering Technique

To study the various eigenmodes of LEE equations, combined Fourier and Laplace transformations can be performed on the LEE equations. For simplicity, only 2D case will be considered. 2D LEE equations for a uniform mean flow in x-direction can be written:

$$\frac{\partial \mathbf{U}}{\partial t} + \frac{\partial \mathbf{E}}{\partial x} + \frac{\partial \mathbf{F}}{\partial x} = \mathbf{S} \tag{1}$$

where $\mathbf{U}$ is the perturbation variables vector and $\mathbf{E}$ and $\mathbf{F}$ are the flux vectors:

$$\mathbf{U} = \begin{pmatrix} \rho' \\ u' \\ v' \\ p' \end{pmatrix}, \quad \mathbf{E} = \begin{pmatrix} \rho_0 u' + \rho' U_0 \\ U_0 u' + p'/\rho_0 \\ U_0 v' \\ U_0 p' + \gamma p_0 u' \end{pmatrix}, \quad \mathbf{F} = \begin{pmatrix} \rho_0 v' \\ 0 \\ p'/\rho_0 \\ \gamma p_0 v' \end{pmatrix} \quad \text{and } \mathbf{S} \text{ is a source.}$$

Taking the Fourier transform of the spatial coordinates and the Laplace transform of the time coordinate in Eq. 1 leads to,

$$\mathbf{A}\tilde{\mathbf{U}} = \tilde{\mathbf{Q}}, \tag{2}$$

where $\tilde{\mathbf{U}}$ is the transform of the primitive variable vectors, $\tilde{\mathbf{Q}}$ is the transformed source term. Hereafter a variable with tilde denotes transformed quantity. The matrix $\mathbf{A}$ and the transformed source vector $\tilde{\mathbf{Q}}$ are given by,

$$\mathbf{A} = \begin{pmatrix} \bar{\omega} - \alpha U_0 & -\rho_0 \alpha & -\rho_0 \beta & 0 \\ 0 & \bar{\omega} - \alpha U_0 & 0 & -\alpha/\rho_0 \\ 0 & 0 & \bar{\omega} - \alpha U_0 & -\beta/\rho_0 \\ 0 & -\gamma p_0 \alpha & -\gamma p_0 \beta & \bar{\omega} - \alpha U_0 \end{pmatrix}$$

and

$$\tilde{\mathbf{Q}} = i \left(\tilde{\mathbf{S}} + \frac{1}{2\pi} \tilde{\mathbf{U}}^*_{initial} \right). \tag{3}$$

Transformations used to derive Equations 2, 3 and 3 are given next. For any scalar function $f(x, y, t)$ the Fourier transform of the spatial coordinates and the Laplace transformation of the time coordinate leads to the transformed $\tilde{f}(\alpha, \beta, \bar{\omega})$, i.e.

$$\tilde{f}(\alpha, \beta, \bar{\omega}) = \int_0^\infty \int \int_{-\infty}^\infty f(x, y, t) \, e^{-i(\alpha x + \beta y - \bar{\omega} t)} dx dy dt, \tag{4}$$

where α and β are the wave numbers related to the spatial coordinates x and y and $\bar{\omega}$ is a complex variable given by,

$$\bar{\omega} = \omega + i\sigma. \tag{5}$$

The real part represents the angular frequency and the imaginary part is a constant. Similarly, following properties of the transformation of the spatial the temporal derivatives have been used:

$$\mathcal{L}\left(\frac{\partial^n f}{\partial x^n}\right) = (i\alpha)^n \tilde{f}, \quad \mathcal{L}\left(\frac{\partial^n f}{\partial x^n}\right) = (i\beta)^n \tilde{f}$$
$$\mathcal{L}\left(\frac{\partial f}{\partial t}\right) = -i\bar{\omega}\tilde{f} - \frac{1}{2\pi} f^*_{initial}. \tag{6}$$

The quantity $f^*_{initial}$ above denotes the Fourier transform of $f(x, y, t)$ at time level $t = 0$ i.e.

$$f^*_{initial}(\alpha, \beta) = \frac{1}{(2\pi)^2} \int \int_{-\infty}^\infty f(x, y, 0) e^{-i(\alpha x + \beta y)} dx dy. \tag{7}$$

Finally, taking the inverse transform of $\tilde{f}(\alpha, \beta, \bar{\omega})$, the scalar function $f(x, y, t)$ can be recovered, i.e.

$$f(x, y, t) = \int \int_{-\infty}^\infty \int_{-\infty+i\sigma}^{\infty+i\sigma} \tilde{f}(\alpha, \beta, \bar{\omega}) e^{i(\alpha x + \beta y - \bar{\omega} t)} d\bar{\omega} d\beta d\alpha. \tag{8}$$

Now going back to Eq. 2, the eigenvalues λ_n and the eigenvectors $\mathbf{y}_n$ of the matrix $\mathbf{A}$ can be expressed as:

$$
\begin{aligned}
\lambda_1 &= \bar{\omega} - \alpha U_0 \\
\lambda_2 &= \bar{\omega} - \alpha U_0 \\
\lambda_3 &= (\bar{\omega} - \alpha U_0) + a_0 \left(\alpha^2 + \beta^2\right)^{1/2} \\
\lambda_4 &= (\bar{\omega} - \alpha U_0) - a_0 \left(\alpha^2 + \beta^2\right)^{1/2}
\end{aligned}
\tag{9}
$$

$$
\mathbf{y}_1 = \begin{pmatrix} 1 \\ 0 \\ 0 \\ 0 \end{pmatrix}, \quad
\mathbf{y}_2 = \begin{pmatrix} 0 \\ \beta \\ -\alpha \\ 0 \end{pmatrix},
$$

$$
\mathbf{y}_3 = \begin{pmatrix} a_0^{-2} \\ -\alpha/\delta \\ -\beta/\delta \\ 1 \end{pmatrix}, \quad
\mathbf{y}_4 = \begin{pmatrix} a_0^{-2} \\ \alpha/\delta \\ \beta/\delta \\ 1 \end{pmatrix}
$$

with $\delta = \rho_0 a_0 \left(\alpha^2 + \beta^2\right)^{1/2}$.

From above relations, it can be clearly seen that the first eigenvector is related to a convection mode of the density and hence represents the entropy mode. The second eigenvector represents the velocity disturbances and is related to a vorticity mode. The last two eigenvectors are related to acoustic modes. In general the transform of the vector of the primitive variables can be expressed as a linear combination of the eigenvectors, i.e.,

$$
\tilde{\mathbf{U}} = \frac{C_1}{\lambda_1}\mathbf{y}_1 + \frac{C_2}{\lambda_2}\mathbf{y}_2 + \frac{C_3}{\lambda_3}\mathbf{y}_3 + \frac{C_4}{\lambda_4}\mathbf{y}_4,
\tag{10}
$$

where the columns of the matrix $\mathbf{Y}$ are the eigenvectors $\mathbf{y}_n$. Again from Equations 2 and 10 applying the similarity transformation $\mathbf{A} = \mathbf{Y}\Lambda\mathbf{Y}^{-1}$, the components C_n of the vector $\mathbf{C}$ which describe the response of the various eigenmodes due to the source $\tilde{\mathbf{Q}}$ can be evaluated:

$$
\mathbf{YC} = \tilde{\mathbf{Q}}
\tag{11}
$$

and after multiplying with the inverse of $\mathbf{Y}$,

$$\mathbf{C} = \mathbf{Y}^{-1}\tilde{\mathbf{Q}}. \tag{12}$$

Equation 12 is the key to the source filtering technique. A modified vector can be derived from Eq. 12 by dropping all but one component of $\mathbf{C}$ e.g. n^{th} component of eigenmode n. A modified source can be calculated using the modified vector into Eq. 11 which excites only the nth eigenmode of the governing equations. The modified source which excites only the nth eigenmode can be written as:

$$\tilde{\mathbf{Q}}_n = \mathbf{y}_n \left(\mathbf{y}_n^{-1}\right)^T \tilde{\mathbf{Q}} \tag{13}$$

In Eq. 13 the dyadic product $\mathbf{y}_n \left(\mathbf{y}_n^{-1}\right)^T$ is a filtering matrix which only excites the nth eigenmode. Using the result of Eq. 13 a combined acoustic filtering matrix $\mathbf{X}$ for the two acoustic modes $\mathbf{y}_3$ and $\mathbf{y}_4$ follows:

$$\mathbf{X} = \mathbf{y}_3 \left(\mathbf{y}_3^{-1}\right)^T + \mathbf{y}_4 \left(\mathbf{y}_4^{-1}\right)^T \tag{14}$$

i.e.,

$$\mathbf{X} = \begin{pmatrix} 0 & 0 & 0 & a_0^{-2} \\ 0 & \alpha^2 \left(\alpha^2 + \beta^2\right)^{-1} & \alpha\beta \left(\alpha^2 + \beta^2\right)^{-1} & 0 \\ 0 & \alpha\beta \left(\alpha^2 + \beta^2\right)^{-1} & \beta^2 \left(\alpha^2 + \beta^2\right)^{-1} & 0 \\ 0 & 0 & 0 & 1 \end{pmatrix} \tag{15}$$

Eq. 13 can, then, be used to evaluate the acoustic source vector $\tilde{\mathbf{Q}}^a$ i.e.,

$$\tilde{\mathbf{Q}}^a = \mathbf{X}\tilde{\mathbf{Q}} \tag{16}$$

Now performing the inverse transformation of the acoustic source vector $\tilde{\mathbf{Q}}^a$ into space and time, the filtered source for the acoustic perturbation equation is achieved. Neglecting the initial term $\tilde{\mathbf{U}}^*_{initial}$ in Eq. 3, full source vector can be written as $\tilde{\mathbf{Q}} = i\tilde{\mathbf{S}}$. Then using the acoustic filtering matrix $\mathbf{X}$ in Eq. 16 along with the transformation relations in Eq. 6, a system of equations is obtained, after some manipulations, which relate the components of the filtered source vector $\mathbf{Q}^a$ to

those of the full source vector $\mathbf{Q}$ i.e.,

$$Q_1^a = a_0^{-2} Q_4 \tag{17}$$

$$\nabla^2 Q_2^a = \frac{\partial^2 Q_2}{\partial x^2} + \frac{\partial^2 Q_3}{\partial x \partial y} \tag{18}$$

$$\nabla^2 Q_3^a = \frac{\partial^2 Q_2}{\partial x \partial y} + \frac{\partial^2 Q_3}{\partial y^2} \tag{19}$$

$$Q_4^a = Q_4 \tag{20}$$

The first and the last filtered source are equal except for the factor a_0^{-2}. It is in consistent with the LEE equations where only isentropic pressure and density fluctuations are excited. Hence for the excitation of only acoustic modes, LEE and APE have equivalent continuity and energy equations. To calculate the second and the third component of the filtered source, the solution of Poisson equations is required.

However the solution of Poisson equations is not always necessary to evaluate the remaining source terms. Firstly, the governing equations in primitive variables have to be transformed initially into a system of linear differential equations on the left-hand side with constant coefficients that describe wave propagation in a quiescent or uniformly moving medium. The remaining terms are lumped together as sources on the right-hand side. A system of differential equations satisfying these requirements can be formulated by using the enthalpy h as variable in the governing Navier-Stokes momentum equations:

$$\frac{\partial \mathbf{v}}{\partial t} + \nabla h = -\left(\mathbf{v}.\nabla\right)\mathbf{v} + T\nabla s \tag{21}$$

Relation between the enthalpy and pressure can be written as:

$$\frac{\nabla p}{\rho} = \nabla h - T\nabla s \tag{22}$$

and the perturbation enthalpy is given by,

$$h' = \frac{p'}{\rho_0} + Ts' \tag{23}$$

Using the relations in Eq. 22, Eq. 23 and dropping the non-linear terms in Eq. 21, following equations for the perturbation quantities can be written:

$$\frac{\partial \mathbf{v}'}{\partial t} + (\mathbf{V}_0.\nabla)\,\mathbf{v}' + \left(\mathbf{v}'.\nabla\right)\mathbf{V}_0 + \frac{\nabla p'}{\rho_0} = F \tag{24}$$

where $F = -\left(\mathbf{V}_0.\nabla\right)\mathbf{V}_0 - \left(\mathbf{v}'.\nabla\right)\mathbf{v}' + \bar{T}\nabla s' + T'\nabla\bar{s} + \overline{T'\nabla s}$

Now, using the identity

$(\mathbf{V}_0.\nabla)\,\mathbf{v}' + \left(\mathbf{v}'.\nabla\right)\mathbf{V}_0 = \nabla\left(\mathbf{V}_0.\mathbf{v}'\right) + \omega' \times \mathbf{V}_0 + \omega_0 \times \mathbf{v}'$ along with $\omega = \nabla \times \mathbf{v}$,

APE momentum equation can be written as:

$$\frac{\partial \mathbf{v}'}{\partial t} + \nabla\left(\mathbf{V}_0.\mathbf{v}'\right) + (\mathbf{V}_0.\nabla)\,\mathbf{V}_0 + \frac{\nabla p'}{\rho_0} = S_m \tag{25}$$

Where S_m is the momentum source term.